Structural Studies of Phospho-MurNAc-pentapeptide Translocase and Ternary Complex of a Nav C-Terminal Domain, a Fibroblast Growth Factor Homologous Factor, and Calmodulin

by

Chih-Pin Chung

Department of Biochemistry
Duke University

Date:_____

Approved:

_____
Seok-Yong Lee, Supervisor

_____
Pei Zhou

_____
Geoffrey Pitt

_____
Leonard Spicer

Dissertation submitted in partial fulfillment of
the requirements for the degree of Doctor
of Philosophy in the Department of
Biochemistry in the Graduate School
of Duke University
2013

ABSTRACT

Structural Studies of Phospho -MurNAc-pentapeptide Translocase and Ternary Complex of a Nav C-Terminal Domain, a Fibroblast Growth Factor Homologous Factor, and Calmodulin

by

Chih-Pin Chung

Department of Biochemistry

Duke University

Date:_____

Approved:

_____

Seok-Yong Lee, Supervisor

_____

Pei Zhou

_____

Geoffrey Pitt

_____

Leonard Spicer

Dissertation submitted in partial fulfillment of
the requirements for the degree of Doctor
of Philosophy in the Department of
Biochemistry in the Graduate School
of Duke University
2013

Abstract

Phospho-MurNAc-pentapeptide translocase (MraY) is a conserved membrane-spanning enzyme involved in the biosynthesis of bacterial cell walls. MraY generates lipid I by transferring the phospho-MurNAc-pentapeptide to the lipid carrier undecaprenyl-phosphate. MraY is a primary target for antibiotic development because it is essential in peptidoglycan synthesis and targeted by 5 classes of natural product antibiotics. The structure of this enzyme will provide insight into the catalytic mechanism as well as a platform for future antibiotic development. MraY genes from 19 bacteria were cloned, expressed, purified and assayed for biochemical stability. The initial crystallization screening revealed that MraY from *Aquifex aeolicus* ($MraY_{AA}$) produced diffracting crystals. Recombinant $MraY_{AA}$ is functional and shows inhibition by the natural inhibitor capuramycin. After extensive optimization of crystallization conditions, the resolution limit of the crystal was extended to 3.3 Å. The crystal structure presented here is the first structure of a member of the polyprenyl-phosphate N-acetyl hexosamine 1-phosphate transferase (PNPT) superfamily. This structure together with our functional dataallows us to identify the location of Mg^{2+} at the active site and the putative binding sites of both substrates. My crystallographic studies provide insights into the mechanism of how MraY attaches a building block of peptidoglycan to the carrier lipid.

Voltage-gated Na^+ (Na_V) channels initiate action potentials in neurons and cardiac myocytes. Na_V channels are composed of a transmembrane domain responsible for voltage-dependent Na^+ conduction and a cytosolic C-terminal domain (CTD) that

regulates channel function through interactions with many auxiliary proteins including members of the fibroblast growth factor homologous factor (FHF) family and calmodulin (CaM). Incollaboration withGeoffrey Pitt's lab, we report the first crystal structure of the ternary complex of the human $Na_V1.5$ CTD, FGF13, and Ca^{2+}-free CaM at 2.2 Å**.** Combined with functional experiments based on structural insights, we present a platform to understand the roles of these auxiliary proteins in Na_V channel regulation and the molecular basis of mutations that lead to neuronal and cardiac diseases. Furthermore, we identify a critical interaction that contributes to the specificity between individual Na_V CTD isoforms and distinctive FHFs.

Contents

List Of Figures

List Of Tables

1 Structural Studies Of Phospho-MurNAc-Pentapeptide Translocase (MraY)

1.1 Summary

The Phospho-MurNAc-pentapeptide translocase (MraY) is a prokaryotic membrane-spanning enzyme responsible for the transfer of the precursor phosphor-MurNAc-pentapeptide to the carrier lipid undecaprenyl phosphate (C_{55}-P), an essential process of peptidoglycan synthesis. MraY belongs to a subfamily of the polyprenyl-phosphate *N*-acetyl hexosamine 1-phosphate transferase (PNPT) superfamily whose members are involved in various biological processes including eukaryotic N-linked glycosylation. Because of its essential role and unique presence in bacteria, MraY has been a target for antibiotics development.. Therefore the atomic structure of MraY can provide valuable mechanistic information that can aid in development of new antibiotics. In this project I screened MraY from 19 species for their suitability for crystallization, identified candidate enzymes, crystallized MraY from two species, optimized crystallization conditions and finally solved the crystal structure of MraY from *Aquifex aeolicus* ($MraY_{AA}$) at 3.3 Å resolution. The crystal structure is the first structure of a member of the PNPT superfamily and it offers the first insights in to the architecture of $MraY_{AA}$. The structure, along with our functional studies, allowed us to identify the location of Mg^{2+} at the active site and the putative binding sites of both substrates. In addition, my crystallographic studies also provide insights into the catalytic mechanism of MraY.

1.2 Introduction

1.2.1 Antibiotics Resistance

Since the discovery of Penicillin by Alexandar Fleming in 1928 and the introduction of the first effective antibiotic sulfonamide in 1937, antibiotics have saved billions of lives from bacterial infection. Over the past 70 years, many million tons of antibiotics have been used and spread into the environment. This has put considerable selection pressure on pathogens, which in turn has led to a rise of a multitude of antibiotic resistant pathogenic bacterial strains. The first bacterial strain resistant to sulfonamides was reported in late 1930s and since then a number of mechanisms through which bacteria can develop antibiotic resistance, such as hydrolysis, efflux and altering targeted antibiotics, have been identified. (J. Davies and Davies).

Infection by antibiotic-resistant bacteria has become a severe threat to public health. Each year in the United States, over two million patients get hospital-acquired infections by drug-resistant bacteria such as methicillin-resistant *Staphylococcus aureus* (MRSA), and about 23,000 of the patients die as a consequence. Antibiotic-resistant infections have put a strain on the already overstretched U.S. healthcare system due to the additional cost of extended hospital stays and the requirement for additional medical attention for patients. The surplus medical costs due to antibiotic-resistant infections amount to as high as 20 billion a year (Center for Disease Control and Prevention, 2013). The collateral loss of productivity also costs society around 35 billion annually (Roberts et al. 2009). These

statistics indicate a strong need for research into the development of novel antibiotics and new potential targets.

1.2.2 Bacterial Cell Wall And Peptidoglycan Synthesis

Bacterial cell wall is a mesh-like layer surrounding the plasma membrane that provides the structural integrity to bacteria. It also serves as a pressure vessel against hypotonic pressure caused by higher concentration of intracellular biomass.

Peptidoglycan, which consists of a polysaccharide polymer cross-linked by atypical peptide containing D-amino acids, is the major component of cell wall of both Gram-negative and Gram-positive bacteria. Peptidoglycan biosynthesis starts with acetylation and aminoacylation of a glucose derivative UDP-N-acetylglucosamine (UDP-GlcNAc) by muramyl ligase family (MurA-F) which generates UDP-N-acetylmuramoyl pentapeptide (UDP-MurNAc-pentapeptide) in the cytoplasm. Phospho-MurNAc-pentapeptide from UDP-MurNAc-pentapeptide is subsequently transferred to the lipid carrier undecaprenyl monophosphate (C_{55}-P) by the membrane enzyme MraY to produce lipid I. The peripheral membrane enzyme MurG rapidly turns lipid I into lipid II by adding an acetylglucosamine (GlcNAc). A yet-to-be confirmed flippase (FtsW, RodA or MurJ) flips Lipid II so that the disaccharide and peptide moiety of Lipid II face the periplasmic space. Transglycosylase and transpeptidase carry out the subsequent peptidoglycan cross-linking reactions to produce peptidoglycan mesh layers of cell wall (Figure 1).

Biosynthesis of peptidoglycan has been a well-established target for antibiotic development as demonstrated by several clinically important antibiotics including Penicillin and Vancomycin, both of which are naturally derived. While Penicillin and Vancomycin block steps in the late stages of peptidoglycan biosynthesis, there are many

other antibiotics of natural origin such as Imidazolinones, 4-Phenylpiperidine and 2-Aminotetralones that target the early stages of peptidoglycan biosynthesis (Bugg et al. 2011), suggesting that these early steps might be good targets for the development of novel antibiotics.

Although structures of most muramyl ligase family members, which play a role in the process of peptidoglycan synthesis, have been known for over a decade, the structure of MraY remained elusive until now.

Table 1: List Of The Available Structure For Enzymes Involving Peptidoglycan Biosynthesis

Gene	First PDB year	PDB ID
MurA	1996	1NAW
MurB	1996	1MBT
MurC	2002	1J6U
MurD	1998	1UAG
MurE	2001	1E8C
MurF	2000	1GG4
MraY	2013	4J72
MurG	2000	1F0K
Flippase	?	?

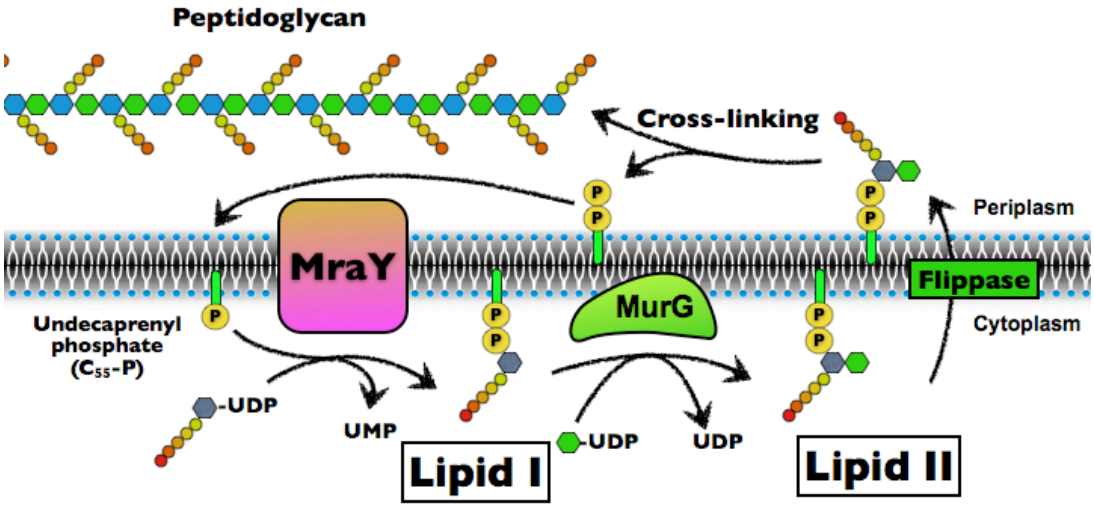

Figure 1: Cartoon Illustration Of The Membrane Steps Of Peptidoglycan Biosynthesis.

Hexagons in blue and green represent MurNAc and GluNAc, representatively, and the five circles attached to blue hexagon represent the pentapeptide. P in yellow circles denotes phosphates. MraY is shown in purple-orange and MurG is colored green-yellow.

1.2.3 Phospho-MurNAc-Pentapeptide Translocase (MraY)

MraY belongs to a subfamily of the polyprenyl-phosphate N-acetyl hexosamine 1-phosphate transferase (PNPT) superfamily. The PNPT superfamily includes the MraY, WecA, TagO, WbcO, WbpL, and RgpG enzyme families that exist in prokaryotes and the GPT (UDP-GlcNAc:dolichol-P GlcNAc-1-P transferase) enzyme family that is responsible for the committed step of N-linked glycosylation in eukaryotes (Lehrman 1994). PNPT superfamily members have varying substrate specificities but share the common function of the transfer of sugar-phosphate derivatives to lipid carriers. Despite the importance of the enzyme superfamily in various biological processes, the structural basis of enzyme function had been elusive due to the complete absence of structural information.

MraY is an integral membrane protein that catalyzes the transfer of hydrophilic phospho-MurNAc-pentapeptide to the lipid carrier undecaprenyl phosphate (C_{55}-P), yielding undecaprenyl-pyrophosphoryl-MurNAc-pentapeptide, also known as Lipid I. This is the first and an essential membrane step of peptidoglycan biosynthesis, and as a result the inhibition of MraY leads to cell lysis. Several features of MraY make it a very attractive target for the development of antibiotics. Firstly, MraY is unique to bacteria as eukaryotes and archaebacteria lack peptidoglycan. The paralogue of MraY in human is UDP-GlcNAc:Dolichol-P GlcNAc-1-P Transferase that shares ~25% identity to bacterial MraYs in general. Secondly, MraY is the target of five different classes of antibiotics of natural origin including capuramycins and muraymycins, most of which target MraY selectively except for tunicamycin that also targets GPT (Winn et al. 2010).

It is worth noting that capuramycin has high activity against *M. tuberculosis* and multi-drug-resistant *M. Tuberculosis* (MDR-TB), and a capuramycin analog has significant *in vivo* effects against an *M. tuberculosis* mouse model as well as an unusual post-antibiotic effect of 55 h against *M. tuberculosis* (Winn et al. 2010; Elena Bogatcheva 2011; Tia Dubuisson 2010; Nikonenko et al. 2009; Reddy, Einck, and Nacy 2008). In addition, muraymycins have significant antibacterial activity against *Staphylococcus aureus* and *Pseudomonas aeruginosa*, and muraymycin analogs are capable to protect mice against *S. aureus* infection (Tanino et al. 2011; Winn et al. 2010). Thirdly, protein E from bacteriophage phiX174 interacts and inhibits MraY by noncompetitive inhibition thus lysing the bacterial cells (Mendel et al. 2006; Tanaka and Clemons 2012). All of these facts make MraY a promising target for the development of antibiotics.

1.3 Cloning, Expression And Crystallization Screening Of MraY

1.3.1 Introduction

To identify an optimal candidate for crystallization, I performed expression and stability screening of MraY orthologs from 19 different species. I found MraY from *Aquifex aeolicus* ($MraY_{AA}$) a promising candidate for structural and functional studies based on expression levels and biochemical behavior. Previous fusion protein experiments to probe the topology of *Escherichia coli* and *Staphylococcus aureus* MraY suggest that the common structure of MraY has 10 transmembrane helices with periplasmic N- and C-termini (Bouhss et al. 1999). The predicted topology of *Aquifex aeolicus* MraY on the basis of the protein sequence is the periplasmic N- and C- termini topology, consistent with experimental results from *E. coli* and *S. aureus* MraYs. To express $MraY_{AA}$ at appropriate orientation for proper protein folding, I used pET26 expression system including an N-terminal pelB signal peptide that leads the N-termini of nascent proteins to the periplasmic space. An N-terminal MBP fusion, immediately after the pelB signal peptide, was also introduced to improve the expression level of $MraY_{AA}$.

1.3.2 Results

1.3.2.1 MraY From *Aquifex Aeolicus* Is A Good Candidate For Crystallization

MraY orthologs from 19 bacterial species were tested for their suitability for future crystallization studies. Among these 19 bacterial species, 5 species were cloned and 14 species were synthesized (Table 2). Large scale expression of the MraY orthologs was performed in order to assay their biochemical stability for crystallization by size exclusion chromatography (SEC).. The MraY of *Aquifex aeolicus* ($MraY_{AA}$) showed optimal stability based on the size exclusion chromatography profile (Figure 1). To investigate the stability of $MraY_{AA}$ in different detergents, I re-equilibrated purified $MraY_{AA}$ with various detergents before SEC. The result indicates that n-decyl β-D-maltoside (DM) improves the monodispersity of the MraY peak compared with n-Dodecyl β-D-maltoside (DDM, used for protein extraction) and other detergents (Figure 3). $MraY_{AA}$ protein solubilized in DDM and DM was used in the initial crystallization screening (~760 conditions per detergent) and only the $MraY_{AA}$ protein in DM generated the most reproducible crystals which diffracted to a medium resolution (~5 Å) in the crystallization trial.

Table 2: Screening MraY From Various Species

Species	GI
Haemophilus ducreyi 35000HP	33151488
Bacillus halodurans C-125	15615131
Mycobacterium tuberculossis H37Ra	148661972
Vibrio cholerae	229607040
Neisseria gonorrhoeae	59718768
Pseudomonas aeruginosa PA01	15599611
Aquifex aeolicus	15605650
Desulfovibrio magneticus	239907966
delta proteobacterium MLMS-1	93454927
Sulfurihydrogenibium yellowstonense SS-5	237691819
Hydrogenivirga sp. 128-5-R1-1	495561292
Thermocrinis albus DSM 14484	289182259
uncultured Desulfobacterium sp.	308271437
Geobacter sp. M18	322421365
Rhizobium etli	190892586
Thermodesulfobacterium geofontis	334902232
Xanthomonas axonopodis pv. citri	21241547
Hydrogenobaculum	195953558
Thermovibrio ammonificans	503302552

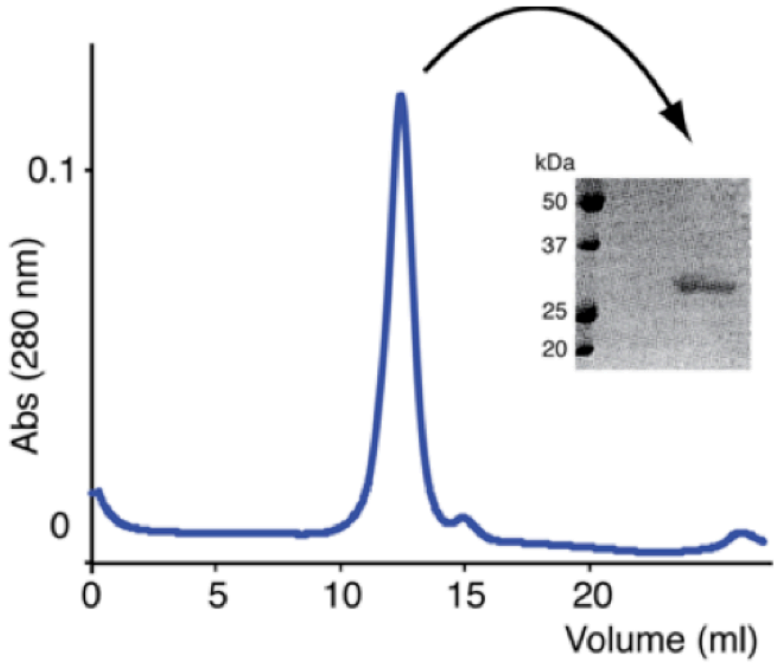

Figure 2: Size-exclusion chromatography profile of $MraY_{AA}$.

Inset shows Coomassie-stained SDS-PAGE of the peak fractions with molecular weight markers indicated on the left.

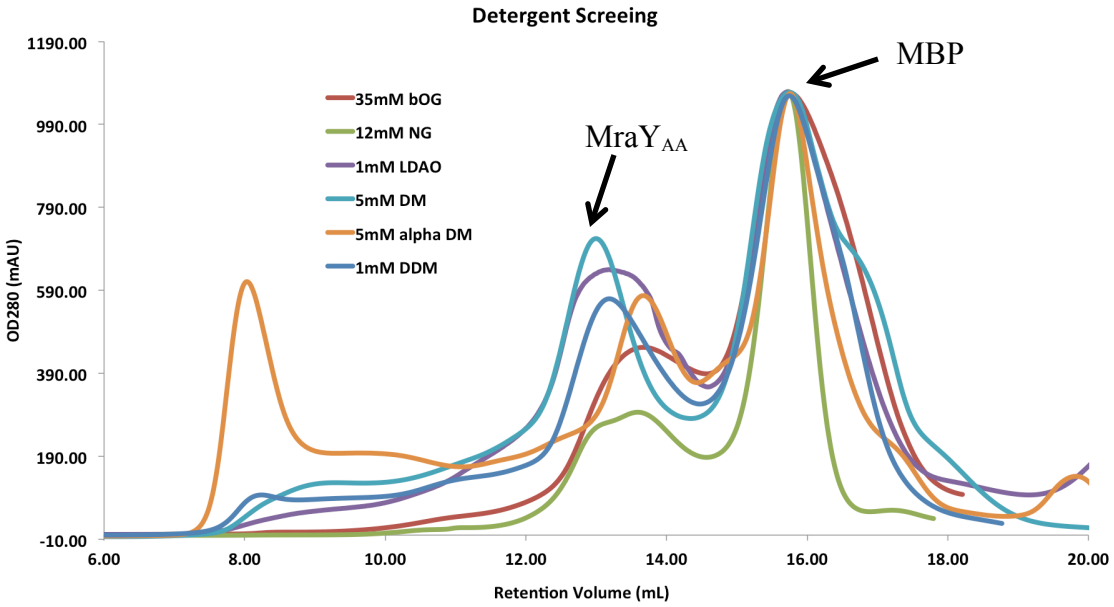

Figure 3: Size-exclusion chromatography profile of $MraY_{AA}$ With Various Detergents.

Equal amounts of $MraY_{AA}$ protein were equilibrated with various detergents above critical micelle concentration (CMC) for 1 hr before the size-exclusion chromatography experiment (Superdex 200). Detergents used in screening were 35 mM *n*-Octyl-β-D-Glucoside (βOG, red), 12 mM Lauryl Maltose Neopentyl Glycol (NG, green) 1 mM Lauryldimethylamine-N-Oxide (LDAO, purple), 5 mM *n*-Decyl-β-D-Maltoside (DM, cyan), 5 mM *n*-Decyl-α-D-Maltoside (alpha DM, orange), 1 mM *n*-Dodecyl-β-D-Maltoside (DDM, blue). All profiles are normalized base on the peak corresponding to maltose binding protein (MBP) at 15.8 ml. $MraY_{AA}$ eluted at 13ml. $MraY_{AA}$ in *n*-Decyl-β-D-Maltoside (DM, cyan) showed the most monodisperse profile.

1.3.3 Materials And Methods

1.3.3.1 Protein Expression And Purification

MraY genes from 19 species (cloned from genomic DNA or synthesized, Table 2) were sub-cloned into a pET26 expression vector including an N-terminal pelB signal peptide that leads the N-terminus of nascent protein to the periplasmic space. The MraY protein was expressed in C41 (DE3) cells in terrific broth as a fusion with a decahistidine-maltose binding protein (His-MBP) followed by a PreScission protease site between the MraY and His-MBP segments. The expression was induced with 0.4 mM IPTG at OD_{600} = 0.8~1 and 20°C for 16 hrs. The harvested cells were resuspended and the fusion protein was extracted from membranes by 30 mM dodecyl-maltoside and purified using a Co^{2+}-affinity column. The His-MBP was then removed from MraY by overnight PreScission protease cleavage. MraY was further purified to homogeneity using size exclusion chromatography (SEC) (Superdex 200, GE healthcare). The solubility and stability of purified MraY proteins were evaluated from the SEC profiles.

The expression of SeMet-substituted $MraY_{AA}$ was induced at 37°C for16 hrs using auto-induction as reported (Fox and Blommel 2009). Methods for purification and crystallization of SeMet-$MraY_{AA}$ were similar to those of $MraY_{AA}$.

1.4 Structure Determination Of *Aquifex Aeolicus* MraY ($MraY_{AA}$)

1.4.1 Introduction

To understand the mechanism of the first step of peptidoglycan biosynthesis by MraY, I determined the structure of $MraY_{AA}$. The structure provides the first insight into the overall architecture and the active site of this class of enzymes.. In addition, the structure reveals the location of Mg^{2+} coordination sites within the enzyme, which is essential for the catalytic activity of MraY (Bouhss et al. 2008),. MraY is predicted to have 10 transmembrane helices with the predicted N- and C-termini located in the periplasmic space. Previous studies indicated that the active site is largely composed of five cytoplasmic loops (A-E) (Figure 4) which contain functionally important and highly conserved amino acids. (Bouhss et al. 2008). Because these amino acids in the cytoplasmic loops are highly conserved among the MraY family, there is a very low incidence of species-dependent inhibition by antibiotics of natural origin (natural product inhibitors) as well as species-dependent variation of substrate specificity (Bouhss et al. 1999; Winn et al. 2010). $MraY_{AA}$ shows high sequence conservation in the cytoplasmic loops with the other members of the MraY family.

Following the optimization of the expression and purification conditions, crystallization experiments were undertaken which resulted in crystals of $MraY_{AA}$ that diffracted to 3.3 Å Bragg spacings. This data was used to build and refine the $MraY_{AA}$ model. In order to increase the accuracy of this data, a number of site-specific methionine mutations were

introduced into the wildtype $MraY_{AA}$. This mutant protein was used to obtain a SeMet-substituted crystal, which enabled single anomalous dispersion (SAD) phasing to 3.9 Å. The methionine mutations served as markers for building of the $MraY_{AA}$ model.

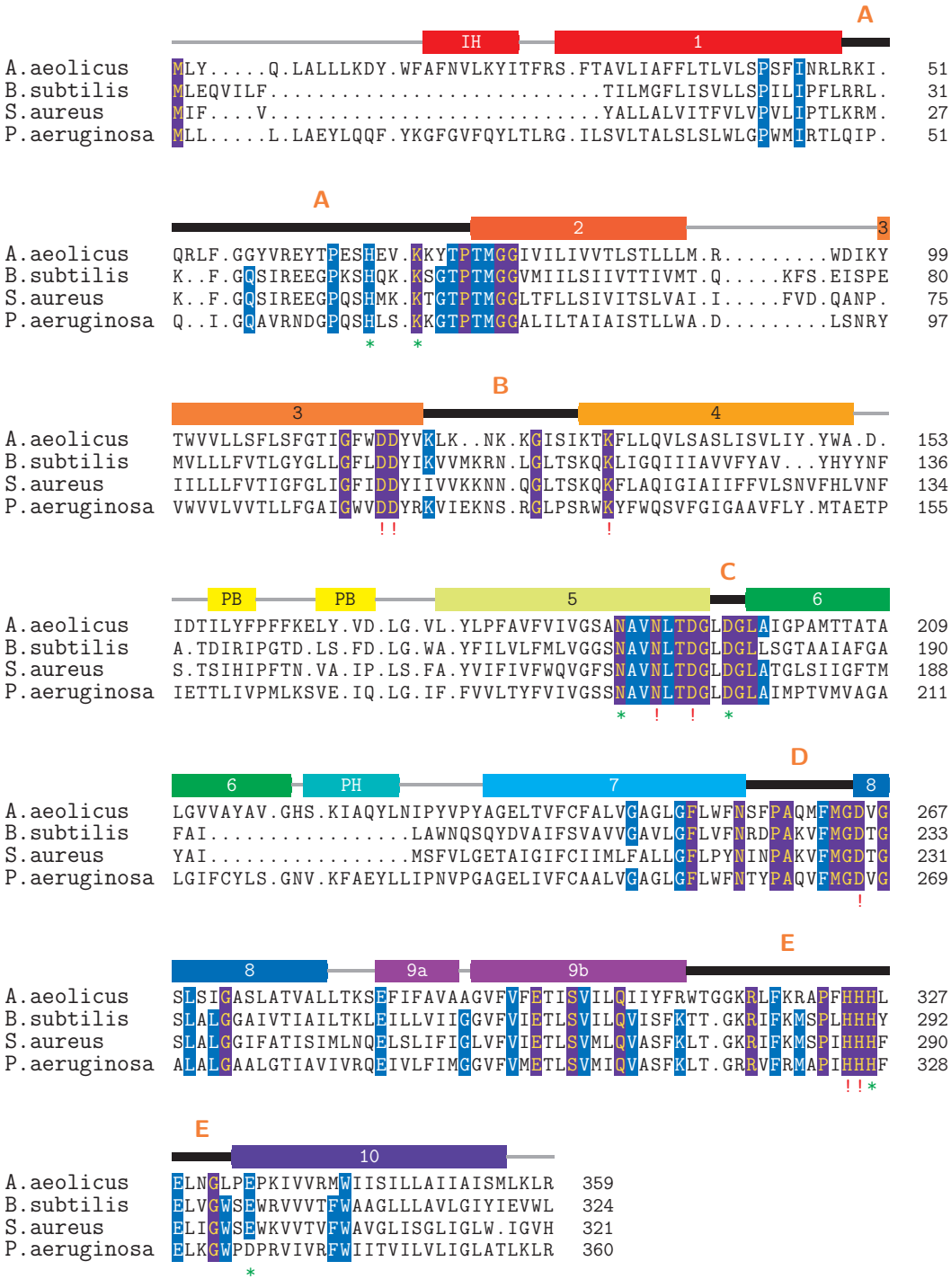

Figure 4: The Intracellular Region Of MraY Is Highly Conserved

MraY Sequence alignment. Highly conserved positions across the MraY family are highlighted in purple (100% identity) and blue (>70% identity) based on 28 MraY orthologs. Secondary structures are shown above the sequence with the same color-coding as Figure 5. The residues with red exclamation marks are essential amino acids for MraY function as mutations at these positions are lethal to bacteria, while mutations of the residues with green asterisks lowered enzyme activity significantly (Al-Dabbagh et al. 2008). The species that were used for the sequence alignment are: *Aquifex Aeolicus* (GI:15605650), *Rickettsia prowazekii* (386082453), *Pseudomonas aeruginosa* (10719754), *Yersinia pestis* (115346359), *Bacillus anthracis* (227813177), *Escherichia coli* (332341419), *Bordetella pertussis* (33564031), *Shigella dysenteriae* (82775494), *Bacillus subtilis* (40163), *Aggregatibacter actinomycetemcomitans* (261867477), *Haemophilus influenzae* (68249684), *Streptococcus pneumoniae* (379070587), *Clostridium acetobutylicum* (15025117), *Staphylococcus aureus* (384861776), *Neisseria meningitidis* (254805550), *Acinetobacter baumannii* (407189484), *Neisseria gonorrhoeae* (59718768), *Streptococcus pyogenes* (383494372), *Enterococcus hirae* (3122385), *Borrelia burgdorferi* (1165287), *Helicobacter pylori* (385220721), *Chlamydia trachomatis* (237803187), *Porphyromonas gingivalis* (334147487), *Enterococcus faecalis* (2149904), *Campylobacter jejuni* (112359797), *Mycobacterium tuberculosis* (494700591), *Synechocystis sp - PCC 6803*(1006612), *Mycobacterium leprae* (130092981).

Results

1.4.1.1 Overall Architecture

$MraY_{AA}$ crystallizes as a dimer in the asymmetric unit. The two-fold axis of the dimer is perpendicular to the putative membrane plane and parallel to one of the crystallographic two-fold axes. When viewed parallel to the membrane, the transmembrane region of the MraY dimer is about 28 Å in height judging from the locations of hydrophobic side chains of the transmembrane helices. Extensions of the transmembrane helices and connecting loops protrude about 13 Å into the intracellular side. When viewed from the periplasmic side, a β-hairpin and a α-helix extend about 11 Å above the transmembrane region. The overall dimensions of the dimer are about 72 Å across the long axis and 55 Å across the short axis when viewed from the cytoplasmic side (Figure 5A-B). Two partial C_{55}-P molecules, built into the model using C_{50}-P, are surrounded by MraY at the dimer interface with their phosphates oriented toward the periplasmic side (Figure 5). Each protomer contains ten transmembrane helices (TM1-TM10), an interfacial helix (IH), a periplasmic β hairpin (PB), a periplasmic helix (PH), and five cytoplasmic loops (Loop A – Loop E). Both the N- and C-termini of the structure are located on the periplasmic side (Figure 5C), which is consistent with previous topological studies (Bouhss et al. 1999). The transmembrane helices pack against each other with various lengths and tilts. TM9 noticeably breaks into two helical fragments (TM9a and TM9b) with TM9b displaying a significant bend (~ 50° relative to the membrane normal) in the middle of the membrane. This bending causes TM9b to protrude ~20 Å into the lipid membrane away from the rest

of structure. This protrusion is buttressed by interactions with TM5. TM9b, together with TM3, TM4, and TM8, surround TM5 and thus generate a cleft around the inner leaflet membrane region of TM8.

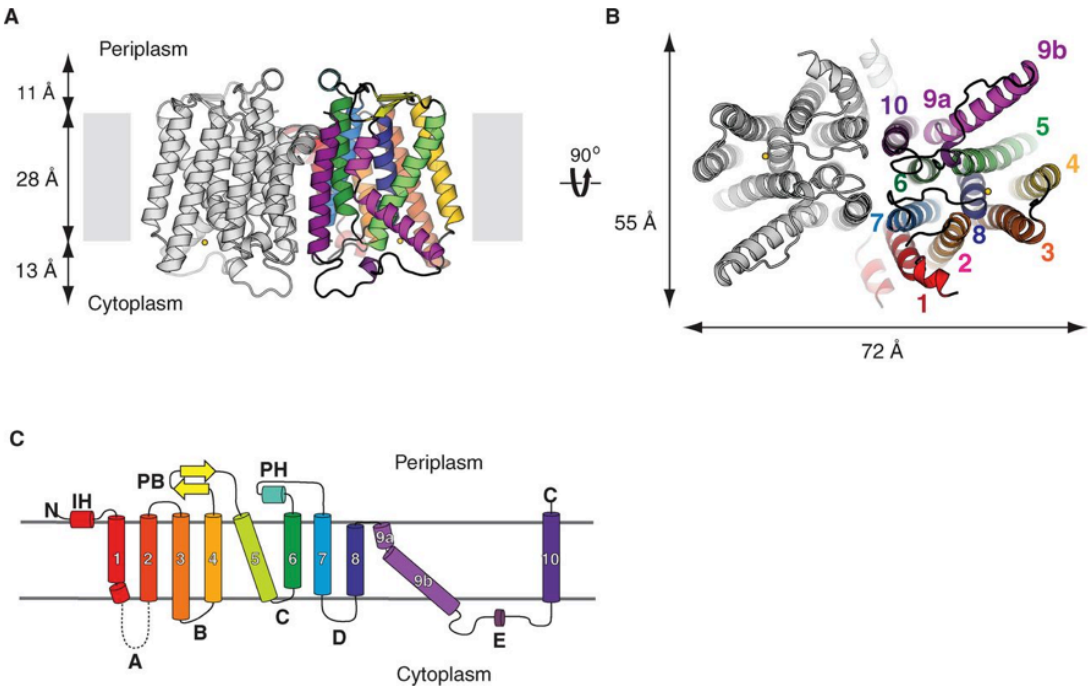

Figure 5: Overall Architecture Of $MraY_{AA}$

(A) View from within the membrane. Only transmembrane helices (TMs) from one protomer are colored. Loop E from both protomers is shown. Mg^{2+} ion is represented as a yellow sphere. **(B)** Cytoplasmic view. Mg^{2+} is shown as a yellow sphere. **(C)** Topology diagram of MraY protomer. Each TM is colored differently. TMs are given numbers, and cytoplasmic loops are given letters. Loop A is missing in the structure. The same colors are used for TMs in **(A)** through **(C)**

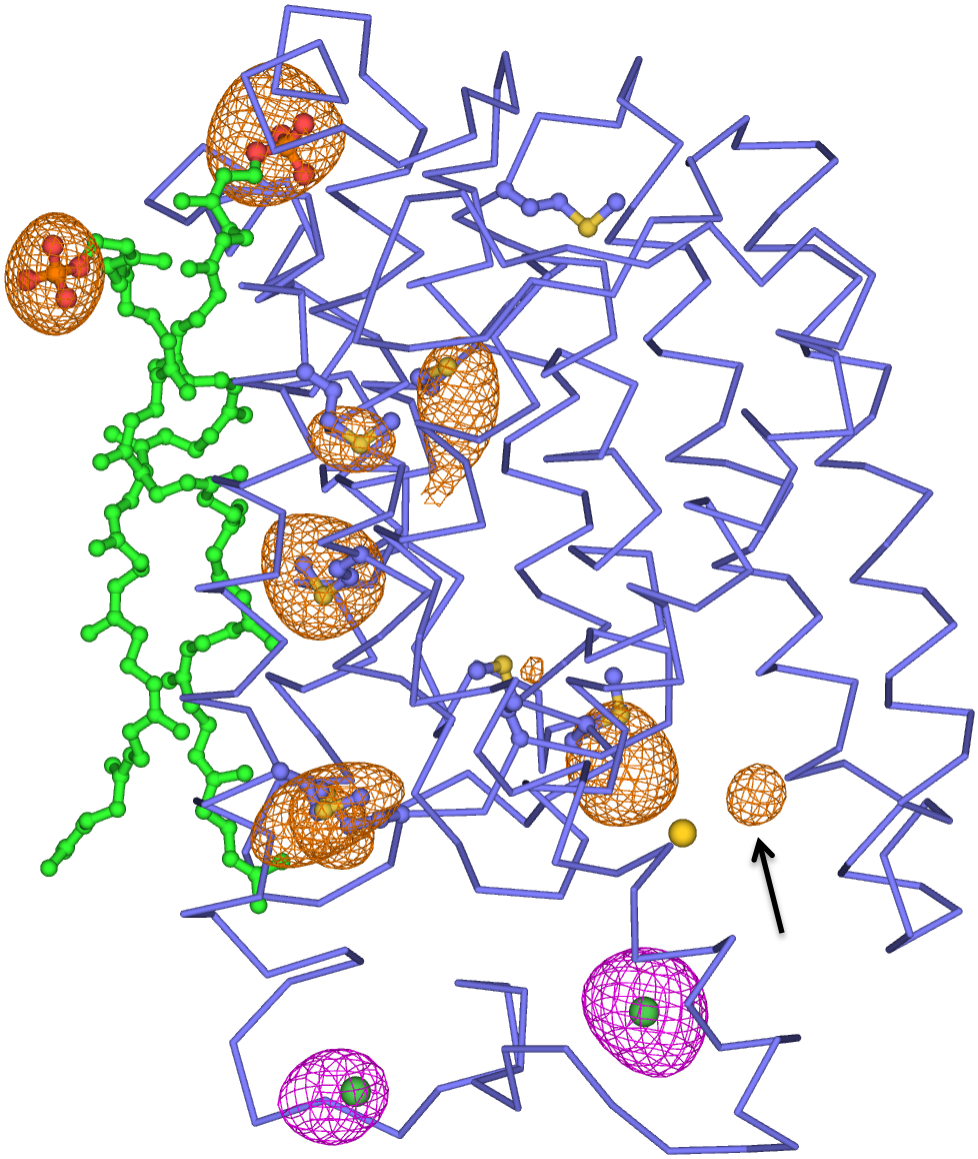

Figure 6: Putative Phosphate Position In The Active Site And C_{55}-P At The Dimer Interface, Together With The Nickel Ion Binding Site At Loop E

Ni^{2+} anomalous difference Fourier map (purple) was calculated from 30 Å - 3.3 Å from data collected from the native crystal grown in the presence of Mg^{2+} and Ni^{2+} using the

model phases. The data was collected at a shorter wavelength (0.975 Å). The anomalous difference peaks, contoured at 5 σ, are shown in magenta mesh

Phosphate and sulfur anomalous difference Fourier map covering one protomer of the MraY dimer is shown. The map was calculated using data from 20 Å- 6.5 Å of the native crystal grown in the presence of Mg^{2+} and Ni^{2+} using the model phases. The anomalous difference peaks, contoured at 3σ, are shown in light brown mesh. Note that five out of seven methionine anomalous difference signals are shown as well as two phosphates from C_{55}-P. The peak that is suggested to correspond to a phosphate within the active site is indicated with an arrow. Mg^{2+} and Ni^{2+} are almost silent in terms of anomalous scattering power at this wavelength (1.55 Å).

Table 3: Data Collection, Phasing And Refinement Statistics.

Data collection	Native	SeMet	Mn^{2+}-co-crystal	Mn^{2+}-soak	Native-long wavelength
Space group	$P2_12_12_1$	$P2_12_12_1$	$C222_1$	$P2_12_12_1$	$P2_12_12_1$
Wavelength (Å)	0.9753	0.9792	1.50	1.55	1.55
Cell dimenstions					
a, b, c (Å)	95.80, 101.49, 138.31	96.20, 101.55, 138.86	97.34,100.50, 141.68	97.28, 100.19, 141.12	96.52, 101.40, 140.06
α, β, γ (°)	90, 90, 90	90, 90, 90	90, 90, 90	90, 90, 90	90, 90, 90
Resolution (Å)	49.08 – 3.3 (3.36 – 3.3)	80.00 – 3.86 (3.93 – 3.86)	50.00 – 5.20 (5.29 – 5.20)	50.00 – 5.70 (5.80 – 6.70)	50.00 – 3.70 (3.76 – 3.70)
Rsym (%)	7.1 (46.7)	9.0 (58.0)	4.5 (64.5)	6.7 (67.3)	11.4 (70.2)
I/σI	35.98 (1.97)	31.10 (2.11)	59.2 (3.8)	56.12 (3.16)	25.34 (2.23)
Completeness (%)	99.5 (97.3)	96.0 (90.0)	99.7 (100)	99.6 (100)	99.7 (99.1)
Redundancy	6.5 (3.6)	10.8 (7.6)	13.6 (13.2)	10.9 (10.4)	13.7 (8.3)
SAD Phasing					
Figure of Merit		0.32 (80–3.9 Å)			
Refinement					
Resolution (Å)	26.7 – 3.3 (3.42 –3.30)				
Completeness (%)*	93.76 (60.0)				
No. of reflections	19537				
R_{work}/R_{free}	21.6/25.8				
Ramachandran (%)					
Favored	96.5				
Outliers	0.2				
R.m.s.d					
Bond lengths (Å)	0.014				
Bond angles (°)	1.3				

$R_{sym} = \Sigma \mid Ii - < Ii > \mid / \Sigma Ii$, where $< Ii >$ is the average intensity of symmetry-equivalent reflections. $R_{work} = \Sigma \mid Fo - Fc \mid / \Sigma \mid Fo \mid$, where Fo and Fc are the observed and calculated structure factors, respectively. R_{free} = R-factor calculated using a subset (~5%) of reflection data chosen randomly and omitted throughout refinement. The figure of merit = |F(hkl)best|/|F(hkl)| and calculated using Phaser before density modification.

*The data treated with ellipsoidal truncation was used for refinement (Adams et al. 2010).

1.4.1.2 Dimer Stoichiometry

To test the oligomeric status of $MraY_{AA}$, cross-linking studies were performed in both detergent micelles and lipid membranes. Treating $MraY_{AA}$ in detergent micelles with increasing concentrations of the amine cross-linker disuccinimidyl suberate (DSS) resulted in an increasing shift in mobility from the predicted size of the monomer to the cross-linked dimer on SDS-PAGE. In the crystallographic dimer, TM10 of one protomer interacts with TM1 and TM7 of the other protomer. Two pairs of cysteine mutations were introduced (T23C/S354C and W253C/R340C) that interact directly at the dimer interface (Figure 7B). Treating membranes containing these cysteine mutants with the membrane-permeable oxidant copper phenanthroline resulted in formation of the disulfide-bridge cross-linked dimer while membranes containing the control mutant with cysteine mutations (I130C) at distal amino acid positions did not, suggesting that $MraY_{AA}$ indeed forms a dimer in the membrane. Consistent with this observation, a recent bacterial two-hybrid study indicated that MraY enzymes in *Caulobacter crescentus* interact with each other (White, Kitich, and Gober 2010). At the center of the dimer interface is a large tunnel. The tunnel, surrounded mostly by hydrophobic amino acids, is oval-shaped with a diameter ranging from 8 Å to 15 Å, large enough to accommodate lipids. Unbiased electron density maps show that there are two elongated electron density peaks that are intertwined within the dimer interface (Figure 8). These density peaks, if continuous, are longer than the depth of the membrane bilayer, rendering them too long to be either phospholipids or detergent molecules. Placement of two partial C_{55}-P molecules (as C_{50}-

P) and subsequent crystallographic refinement reduced the R_{free} of the final model by about 1%. To identify the lipids associated with $MraY_{AA}$ in the crystals, the crystals were washed and dissolved and mass spectrometry was performed. Consistent with our crystallographic observation, mass spectrometry analysis identified C_{55}-P and its derivative undecaprenyl phosphate amino arabinose (C_{55}-P-AraN) in the protein sample derived from the crystals. Also, an anomalous difference Fourier map, calculated from the native crystal at a long wavelength (1.7 Å) using the model phases without C_{55}-P, shows anomalous difference peaks at the phosphate positions of the modeled C_{55}-P molecules (Figure 6). The phosphates from the C_{55}-P molecules are oriented toward the periplasmic side and interact with backbone amides from the N-terminus of TM1 and the side chain hydroxyl of Ser26 (Figure 9). Since the phosphate interacts with the backbone amides of the N-terminus of TM1, the helical dipole of TM1 must be utilized, suggesting that these interactions are structurally conserved. The total buried surface area is 3182 $Å^2$ upon dimerization excluding the C_{55}-P-$MraY_{AA}$ interactions and 4607 $Å^2$ if the interactions are included. Interestingly, amongst the $MraY_{AA}$ orthologs sequence conservation is higher within the dimer interface than the surface away from the interface. Lipids bound to membrane proteins can play important roles either structurally or functionally, however in the case of $MraY_{AA}$ further biochemical and functional studies will be required to identify the exact role of the bound C_{55}-P molecules.

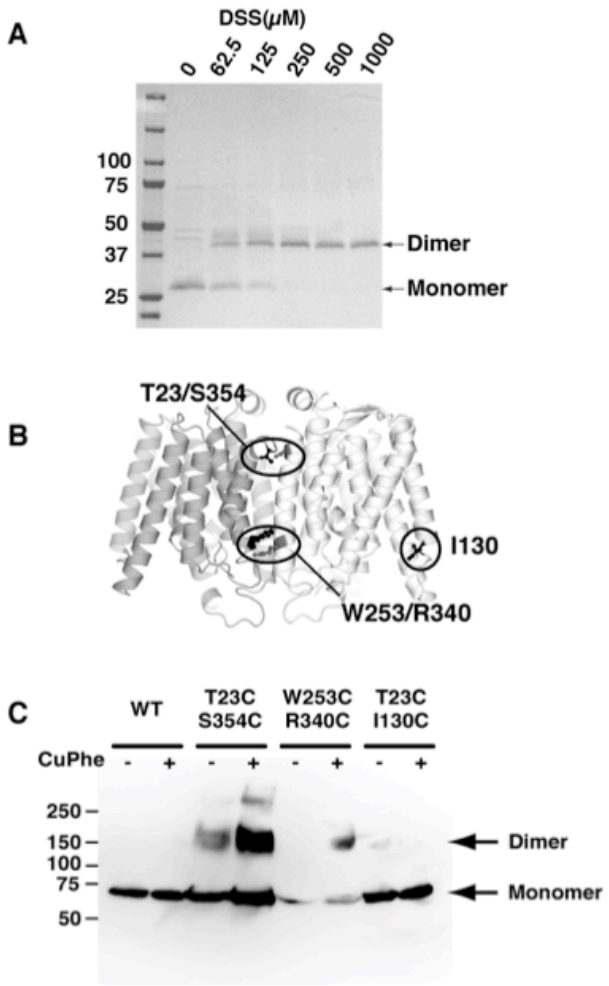

Figure 7: Stoichiometry Of $MraY_{AA}$.

(A) Commassie-stained SDS-PAGE analysis of cross-linking. Purified $MraY_{AA}$ in detergent micelles was treated with increasing concentration of disuccinimidyl suberate (DSS) as indicated above the lanes. **(B)** Dimer interface with the amino acid residues chosen for cysteine mutations indicated with circles. **(C)** Western-blot analysis of cross-linking. Cell membranes containing maltose-binding protein (MBP)-fused $MraY_{AA}$, MBP-$MraY_{AA}$(23C/354C),MBP-$MraY_{AA}$(253C/340C), and the control MBP-$MraY_{AA}$(23C/130C) were treated with and without 200 μM copper phenanthroline (CuPhe). Note that MBP does not contain any endogenous cysteines. Molecular weight markers are indicated on the left in **(A)** and **(C)**. All the cross-linking studies were performed at room temperature and at least for three times independently.

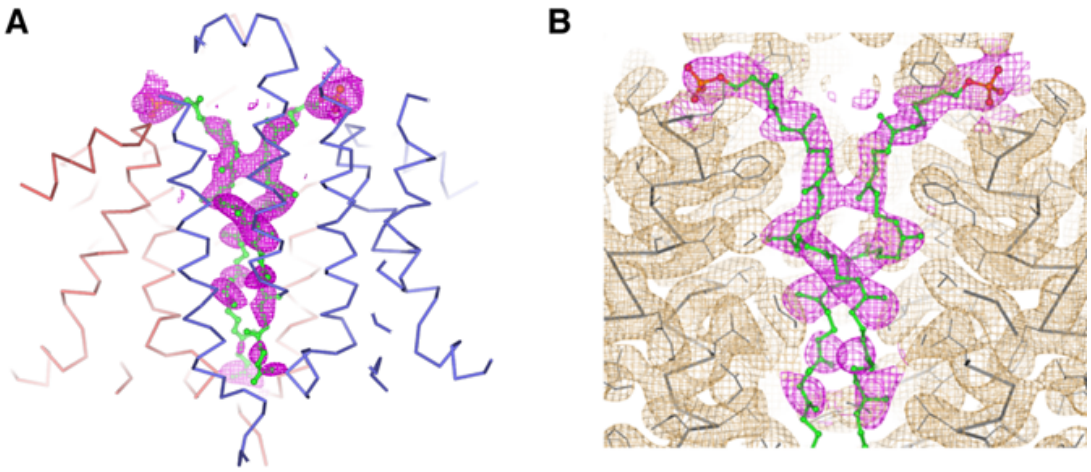

Figure 8: C_{55}-P At The Dimer Interface

(A) An F_O-F_C OMIT map calculated with the final model phases is shown in magenta mesh contoured at 2σ. The partial C_{55}-P model (C_{50}-P) is shown as green sticks. Each protomer is shown as a Cα trace and colored blue and orange, respectively. **(B)** An unbiased two-fold NCS averaged electron density map at 3.3 Å, contoured at 0.9σ, calculated with phases derived from 3.9 Å SAD phasing and a partial model (about 40% of protein). The final model is shown in stick representation. The electron density corresponding to C_{55}-P is shown in magenta for clarity and the C_{55}-P model is shown in ball-and-stick representation.

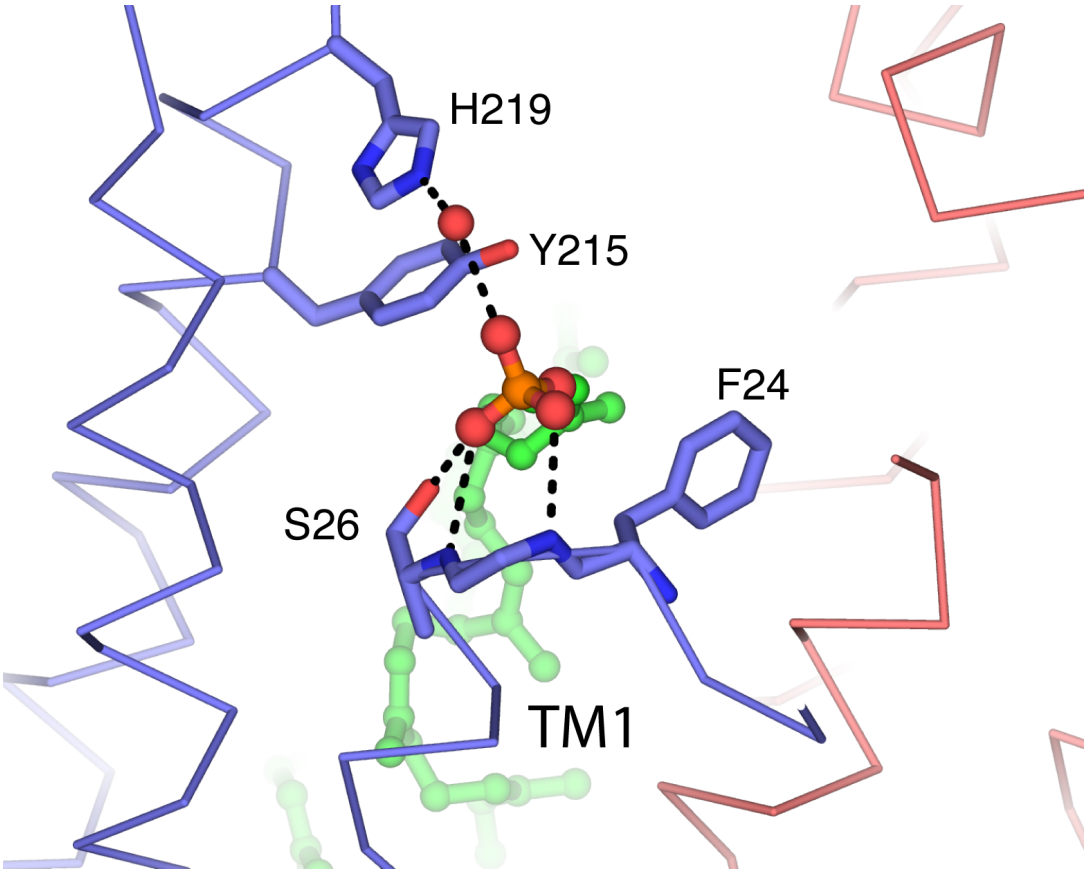

Figure 9: Coordination Of The C_{55}-P Phosphate Moiety At The Dimer Interface.

Side chains of amino acid residues that interact with C_{55}-P are shown in stick representation. The interactions are shown as dotted lines. Phosphate and water (interacting with H219) are shown in red and the undecaprenyl group (C_{55}) is shown in green.

1.4.1.3 Active Site And The Mg^{2+}-Binding Site

To gain functional insight, I mapped sequence conservation and previous mutational data onto the $MraY_{AA}$ structure. The highest conservation is localized around the cleft formed by the cytoplasmic and inner-leaflet membrane regions of TM3, TM4, TM8, and TM9b (Figure 10A). Recent mutational studies of *Bacillus subtilis* MraY showed that fourteen invariant polar/charged amino acid residues are essential as shown by both *in vivo* and *in vitro* enzymatic assays (Al-Dabbagh et al. 2008). Most of these residues are localized in the cleft, indicating that this region serves as the active site. On the basis of our mutational mapping, I predicted that three invariant aspartate residues (Asp117, Asp118, and Asp265) (Figure 10D) conserved throughout the entire PNPT family and two invariant histidine residues (His324 and His325) in the MraY family are catalytically important since they do not appear to be involved in maintaining the putative active site structure. To test our prediction, I individually mutated each of these three invariant aspartates as well as three histidine residues (His324, His325, and His326). Jinshi Zhao and Robert Gillespie in Pei Zhou's laboratory performed the TLC-based MraY functional assay. We found that mutations of any of the three aspartate residues and one histidine residue (His324) resulted in a nearly complete loss of activity of $MraY_{AA}$ while mutating a non-conserved residue (Ile83) away from the active site did not reduce catalytic activity (Figure 10C). These results show that at least three acidic residues and one histidine residue (Asp117, Asp118, Asp265, and His324) (Figure 10D) are catalytically important within the active site of $MraY_{AA}$.

I next identified the Mg^{2+}-binding residues within the active site, as Mg^{2+} is necessary for catalysis. It had been assumed that the residues corresponding to Asp117 and Asp118 in $MraY_{AA}$ are involved in Mg^{2+} coordination based on sequence similarity to the Mg^{2+}-binding motif (DDXXD/N) of prenyl transferases (Lloyd et al. 2004), but this assumption has recently been challenged (Al-Dabbagh et al. 2008). To identify Mg^{2+} within the active site of the structure using X-ray crystallography, I performed anomalous scattering studies using Mn^{2+}-substituted $MraY_{AA}$ crystals (See "Anomalous Scattering" in the Methods and Materials for the details). Anomalous difference Fourier density maps calculated from both Mn^{2+}-soaked and Mn^{2+}-co-crystallized crystals displayed peaks at the active site near Asp265. The Mn^{2+} directly interacts only with Asp265 and a water molecule via Thr75, but not with Asp117 or Asp118. An F_O-F_C OMIT electron density map from the native data at 3.3 Å shows that there are unassigned density peaks within interacting distance of the Mg^{2+}, which are probably involved in Mg^{2+} coordination (Figure 11).

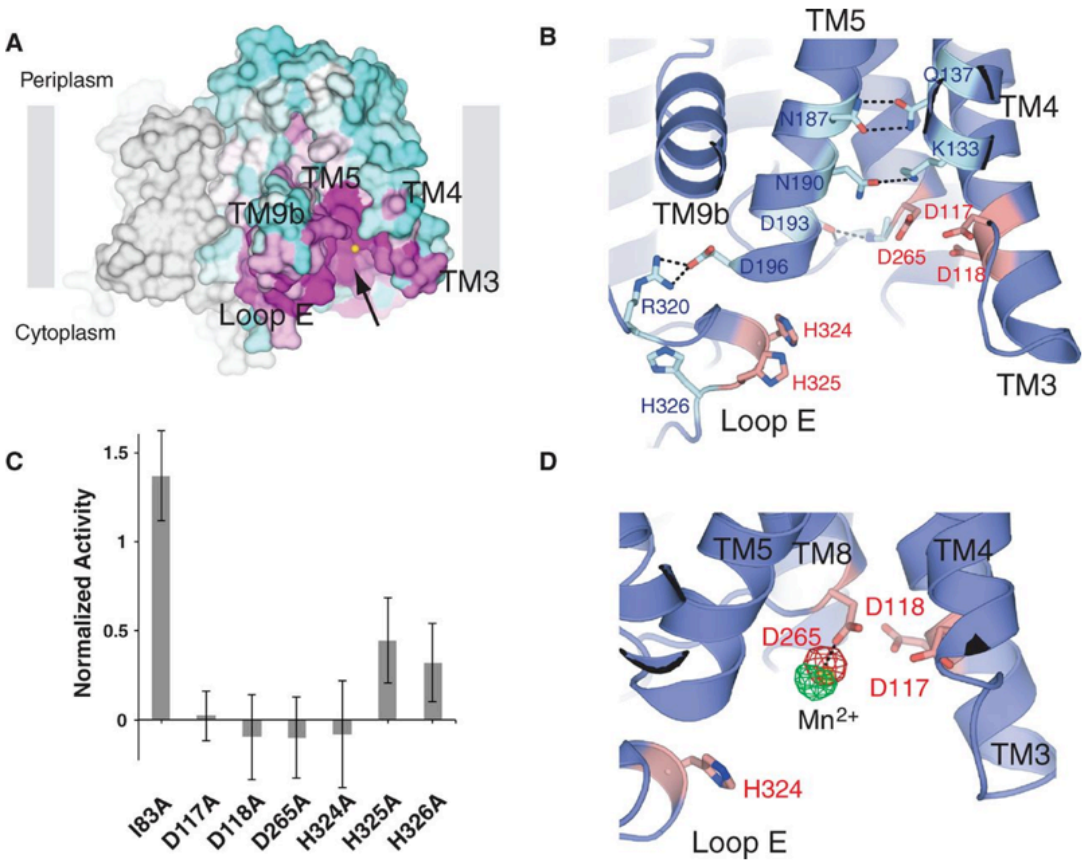

Figure 10: Active Site Of $MraY_{AA}$

(A) Conservation mapping on the $MraY_{AA}$ structure. Sequence conservation is colored on one protomer with a gradient from magenta (absolutely conserved) to cyan (least conserved) based on 28 MraY sequences. The structure is rotated about 45° toward the reader relative to Figure 5A. The arrow indicates the active site cleft. **(B)** Mutation mapping on the $MraY_{AA}$ structure based on previous mutagenesis studies on MraY from *Bacillus subtilis* (Al-Dabbagh et al. 2008). Mutations leading to significant functional effects are shown in stick representation. Among these mutations, amino acid residues that appear to be important for catalysis and active site structural maintenance are colored orange and cyan, respectively. **(C)** Mutational studies of putative active site residues of

$MraY_{AA}$ using the same translocase assay as Figure 20. The specific activities of mutants were normalized to that of wild type (n = 3, SD). **(D)** Active site Mn^{2+} (Mg^{2+})-binding site. Anomalous difference Fourier density for Mn^{2+}, shown in green mesh contoured at 5.2σ, is calculated from a data set collected from a crystal grown in the presence of Mn^{2+} without Ni^{2+} using phases derived from the model without the metals. Another anomalous difference Fourier density peak for Mn^{2+}, shown in red mesh contoured at 3.4σ, was calculated from a data set collected from a crystal soaked with Mn^{2+} in the presence of Ni^{2+} using phases derived from the model without the metals.

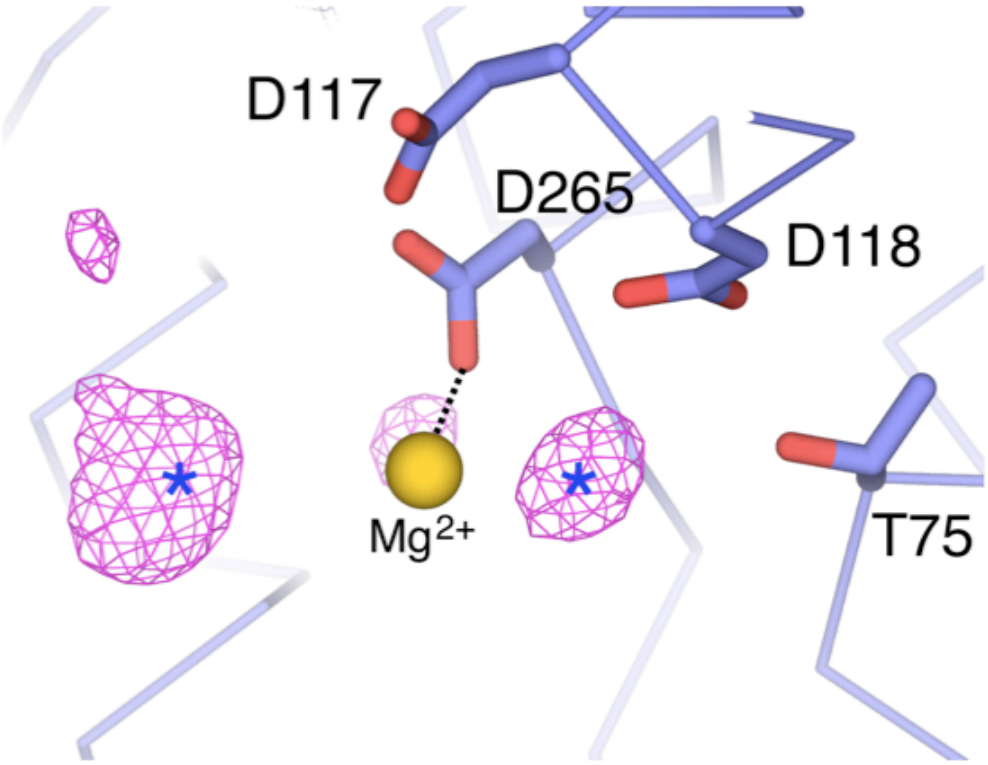

Figure 11: Mg^{2+} Coordination.

An F_O-F_C OMIT map shows that there are two density peaks (marked with blue asterisks) that can participate in coordinating the Mg^{2+} ion in the active site of $MraY_{AA}$. The map was calculated using model and contoured at 3σ.

1.4.1.4 TM9b And Loop E

From sequence conservation and topological studies, it was predicted that MraY contains five conserved cytoplasmic regions that are functionally important. Significant portions of the five predicted cytoplasmic loops correspond to the inner-leaflet membrane region of TM helices in the structure (Figure 4). The fifth predicted loop is composed of TM9b and the loop connecting TM9b to TM10 (loop E). This region also shows subfamily specific sequence conservation within the PNPT superfamily. Since bacterial subfamilies of the PNPT superfamily use different sugar phosphates as substrates, it was predicted that TM9b/loop E has a role in the specific recognition of these sugars. A recent study of WecA, a member of the PNPT superfamily, implicates this region in interacting with sugar nucleotides (Amer and Valvano 2001).

TM9b/loop E surrounds the active site thus making the active site cleft deeper. Within the two protomers of the asymmetric unit, only one (chain A) shows well-resolved electron density for loop E. Loop E is about 23 amino acids long and is composed of several basic residues followed by a stretch of sequence (PXHHHXEXXG) that is highly conserved within the MraY family (hereafter termed "HHH motif"). The HHH motif includes a short stretch of helical segment followed by a loop (Figure 12). It appears that the loop E structure is maintained by the interactions of this HHH motif with TM5 and loop D, particularly the absolutely conserved Phe262 of loop D. The short helical segment within the HHH motif includes the first two histidines (His324 and His325) that coordinate an ion and the third histidine (His326) that, together with Glu328, coordinates a second ion,

as evidenced by an F_O-F_C OMIT electron density map. I verified that both ions in loop E are Ni^{2+} using anomalous diffraction experiments at 0.975Å. The structure of the HHH motif appears to be stabilized by Ni^{2+} coordination. Consistent with this observation, crystals grown in the absence of Ni^{2+} diffract poorly and the electron density for loop E is not well resolved despite very similar crystal packing as the higher-resolution native crystal containing Ni^{2+}. The translocase assay, described in the next chapter, with concentrations of Mg^{2+} (100 mM) and Ni^{2+} (10 mM) used for crystallization, resulted in full activity, suggesting that the structure of Ni^{2+}-bound loop E reflects an active conformation.

How does TM9b/loopE recognize UDP-MurNAc-pentapeptide? TM9b is significantly tilted with respect to the membrane plane and is an amphipathic helix with highly conserved polar and charged amino acids facing the intracellular side. There are not many interactions between TM9b and loop E, resulting in a gap between these regions. An F_O-F_C OMIT map shows a τ -shaped density peak threaded and trapped in the gap between TM9b and loop E (Figure 12). The residues surrounding this density are mainly charged and polar, making it less likely that the density is from either acyl chains of lipids or alkyl chains of detergent molecules. This electrostatic environment between TM9b and loop E hints that the density may correspond to the pentapeptide moiety from either UDP-MurNAc-pentapeptide (Figure 13) or Lipid I. Manual placement of the pentapeptide from UDP-MurNAc-pentapeptide into the density resulted in many satisfactory electrostatic interactions with TM9b/loop E (Figure 12). Although our manual docking cannot give us a unique model for the density due to the resolution limit, it shows us that the length and

the shape of the density is compatible with the pentapeptide moiety. In addition, it provides us with a testable hypothesis that the role of the conserved polar/charged amino acids on TM9b is to interact with the pentapeptide (Figure 10). I have mutated residues on TM9b/loop E and tested their functional effects by the translocase assay. Consistent with our prediction, mutation of the residues interacting with the bound molecule within TM9b/loop E compromised activity of $MraY_{AA}$ while mutations of the residues pointing away from the molecule did not. It is noteworthy that MraY has relatively low specificity for the peptide part of the substrate in general, consistent with our observed mutational effects.

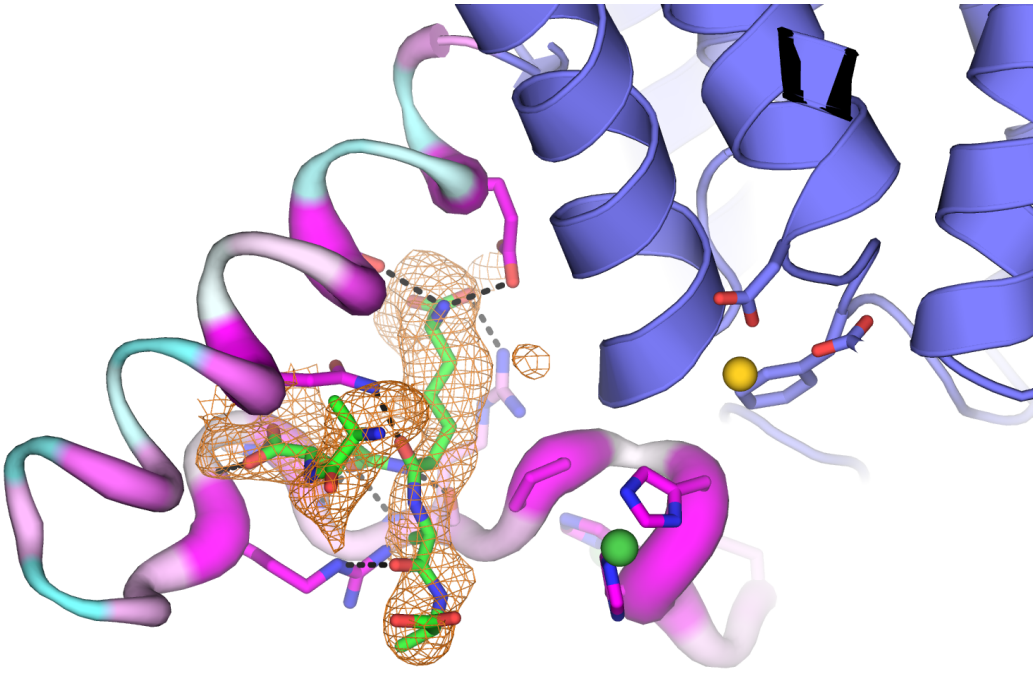

Figure 12: Zoomed-In View Of TM9b/Loop E.

The modeled pentapeptide and its interactions with TM9b/loop E are shown. TM9b/loop E is shown in sausage representation with the thicker region more conserved (magenta) and the thinner region less conserved (cyan). The hypothetical positions of the MurNAc and diphosphate moieties of UDP-MurNAc-pentapeptide are shown as dotted lines. Mg^{2+} is shown as a yellow sphere.

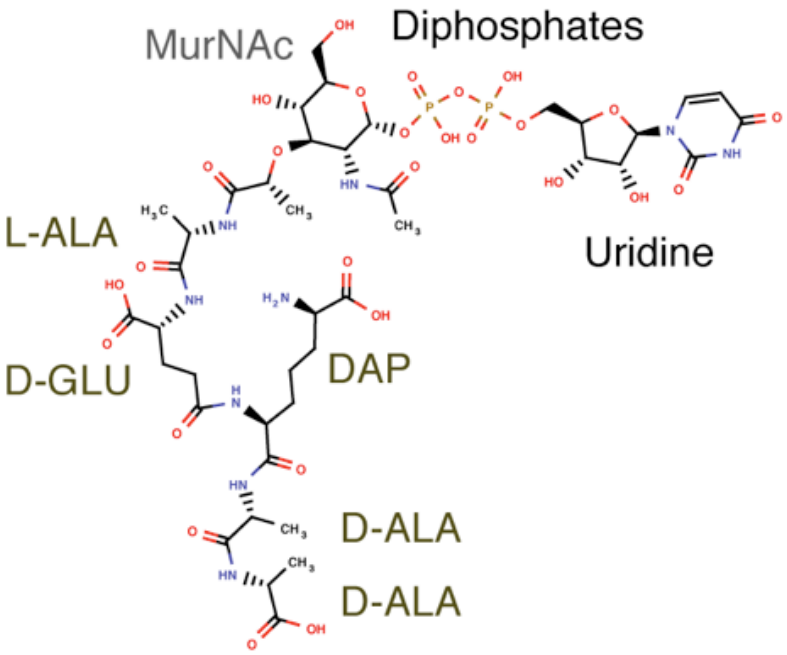

Figure 13: Chemical Structure Of UDP-MurNAc-Pentapeptide

1.4.1.5 Putative C_{55}-P Binding Site And Hypothetical Mechanism

After identifying the putative binding region for UDP-MurNAc-pentapeptide, the next step was to identify the C_{55}-P binding site. The surface representation of $MraY_{AA}$ shows that there is an inverted U-shaped groove surrounding TM9b (Figure 14). An F_O-F_C OMIT map shows residual electron densities in the groove, though they are not entirely connected. Because C_{55}-P must make twists and turns to fit in the membrane due to its length, it appears that the inverted U-shaped groove within the membrane region of the enzyme could serve as the C_{55}-P binding site. We attempted to model a C_{55}-P molecule into the structure. Placement of an undecaprenyl group from C_{55}-P was guided by an F_O-F_C OMIT map. As for the placement of the phosphate group from C_{55}-P, we utilized our crystallographic data and previous functional data. We carried out anomalous scattering studies on a native crystal to identify a phosphate positioned in the active site (Figure 14). The putative phosphate position (purple density) based on an anomalous difference Fourier map is within interacting distance of Asp117 (Asp98 in *Bacillus subtilis* MraY), consistent with a conclusion from the previous biochemical studies from the Bouhss group. In the active site, the phosphate from the C_{55}-P model is within interacting distances of Asp117, Lys121, Lys133, and the Mg^{2+} ion (Figure 14). The presence of both basic and acidic amino acid residues as well as Mg^{2+} makes this region a good candidate for the phosphate-binding site.

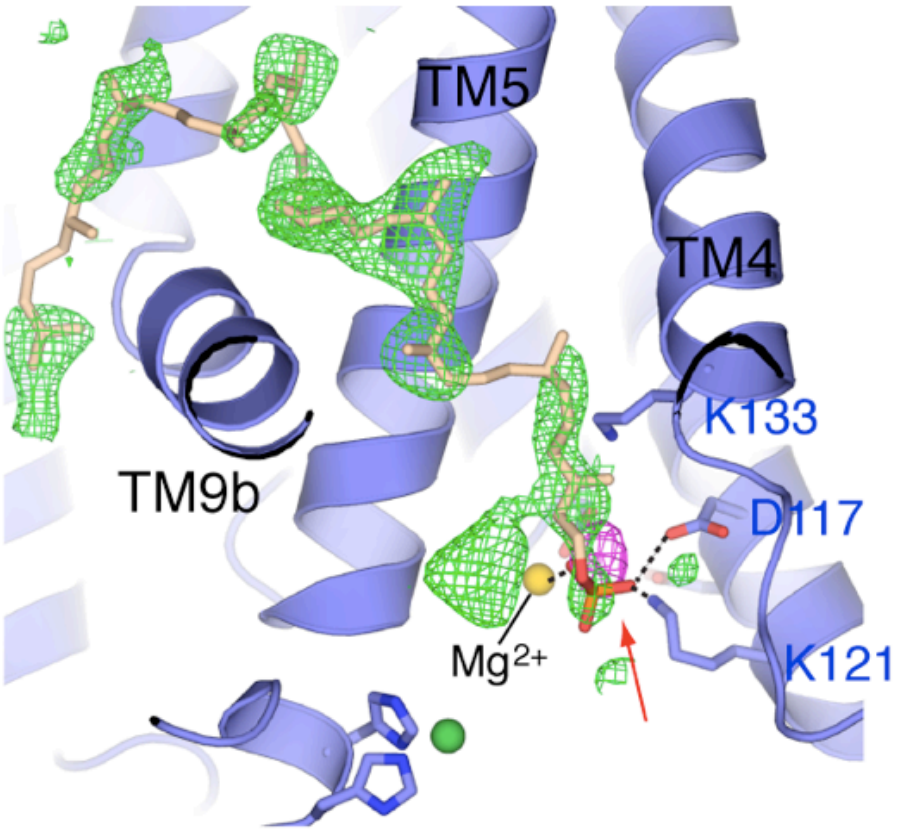

Figure 14: Putative C_{55}-P-Binding Site And C_{55}-P Model.

F_O-F_C OMIT electron density is shown in green mesh and contoured at 2.1σ. Anomalous difference Fourier density for the putative phosphate, shown in magenta mesh contoured at 3Å, was calculated from a data set collected at a wavelength of 1.55 Å from a crystal grown in Mg^{2+} and Ni^{2+} using the phases derived from the model without any substrates or metals.

1.4.2 Materials And Methods

1.4.2.1 Crystallography

Extensive crystallization experimentswere performed using in-house crystallization screen solutions. Crystals from most conditions diffracted poorly (>20 Å), but crystals grown in the presence of Mg^{2+} showed promise with anisotropic diffraction (two directions 4.5 Å and one direction ~7.5 Å). The optimized crystals grew in the following conditions: 8-10 mg/mL $MraY_{AA,}$ in a buffer containing 150 mM sodium chloride, 20 mM Tris pH 8.0, 5 mM DM, and 2 mM DTT, was mixed with a crystallization solution containing 20-120 mM magnesium acetate, 9 mM nickel chloride, 50 mM sodium cacodylate pH 5.6, and 45% PEG400. Crystals appeared within a few days and were fully grown within 7 to 14 days at 17°C. Selenomethionine (SeMet)-substituted MraY crystals were grown in similar conditions with slightly lower protein concentrations. Initial SAD phasing was performed usinga SeMet-MraY crystal that diffracted to 3.9 Å in the ID 24-C beam line at the Advanced Photon Source. SHELX was used to identify 14 selenium (Se) sites (Figure 15A), and Phenix was used to calculate phases using the Se substructures. There are two $MraY_{AA}$ molecules in the asymmetric unit, which allowed us to perform non-crystallographic symmetry averaging as well as solvent flattening at 3.9 Å using RESOLVE from the Phenix package. At this stage, electron density for many transmembrane helices was discernible and allowed us to place idealized poly-alanine helical fragments manually (Figure 15B). With this partial model, I calculated phases from a combination of molecular replacement and single anomalous dispersion (MR-

SAD), which improved the phases significantly (Figure 15C). The 3.3 Å native data was subjected to ellipsoidal truncation and anisotropic scaling before phase extension and refinement using the UCLA diffraction anisotropy server. All the Se positions were identified by an anomalous difference Fourier map, which guided model building. To further help model building, a mutant SeMet crystal (L105M) was grown and the introduced methionine was identified by an anomalous difference Fourier map (Figure 15A). The structural model of $MraY_{AA}$ was built both manually and using the automatic model-building software AutoBuild from Phenix. The final model was refined to R_{work}/R_{free} = 22.3/26.5 % with good geometry and contains amino acids 14 – 48, 70 –357 for one protomer (chain A) and 14 – 48, 70 –121, 126–311, 334–357 for the other protomer (chain B), two Mg^{2+} ions, and two Ni^{2+} ions.

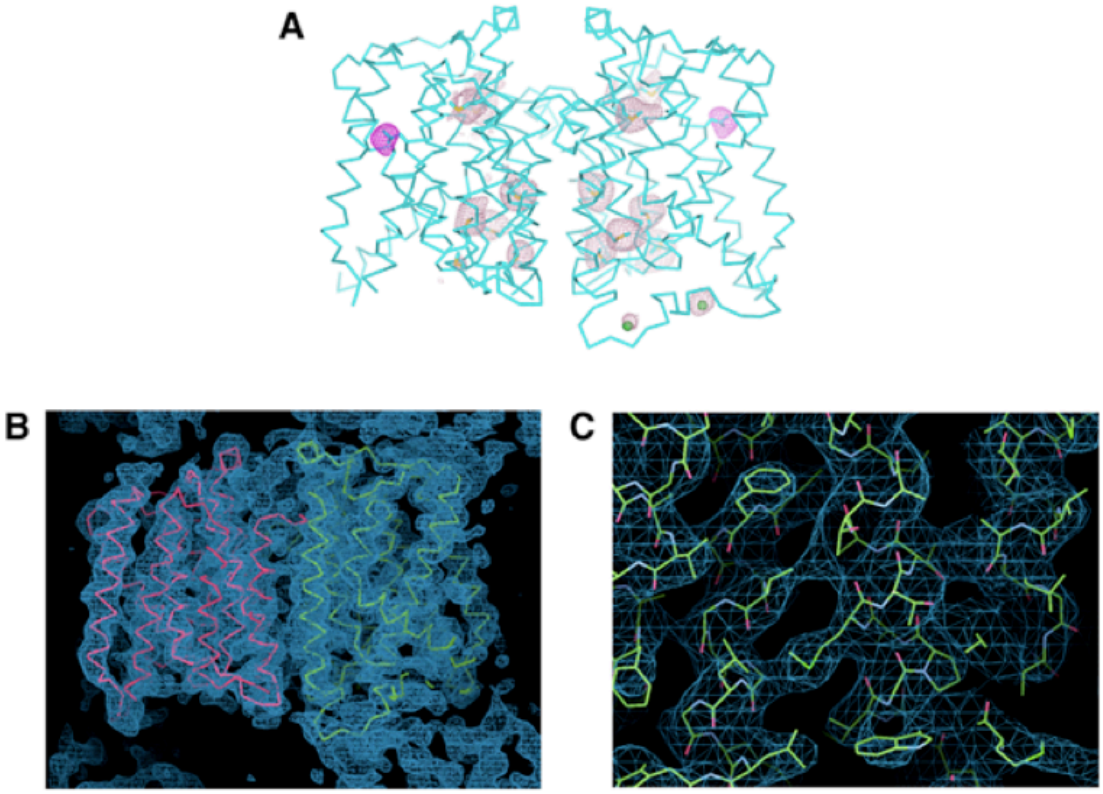

Figure 15: Phasing And Model Building

(A) Anomalous difference Fourier density peaks for Se and Ni^{2+} ions (green sphere) are shown in salmon mesh (2.5σ). The map was calculated using the SAD phasing from the SeMet data using diffractions at 40 Å to 3.9 Å. The final model was shown in Cα representation with all 14 methionines shown in stick representations. The anomalous difference Fourier density peaks for the introduced mutation (L105M) are shown in pink mesh, contoured at 3σ. **(B)** Electron density map of $MraY_{AA}$ at 3.9 Å. The partial model of the $MraY_{AA}$ dimer in the asymmetric unit is shown in green and magenta. The map was calculated from SeMet SAD phasing followed by two-fold non-crystallographic

symmetry (NCS) averaging. (C) Zoomed-in view of the two-fold NCS averaged electron density map at 3.3 Å. A partial model with sidechains was built into the electron density map. The SeMet-SAD phases together with the partial model phases at 3.9 Å were extended to 3.3 Å during two-fold non-crystallographic averaging.

1.4.2.2 Anomalous Scattering

All the data for anomalous scattering studies were collected at the BM22 beamline at the Advanced Photon Source. To identify the position of Mg^{2+}, I prepared two types of crystals. The best-diffracting $MraY_{AA}$ crystal form requires both Mg^{2+} and Ni^{2+} for successful growth. Co-crystallization of MraY crystals with Mn^{2+} and Ni^{2+} was not successful; therefore I replaced Mg^{2+} in the crystals with Mn^{2+} by soaking the native crystal in a Mn^{2+}-containing mother liquor. To replace Mg^{2+} with Mn^{2+}, about half of the drop solution was removed and 2 μL of crystallization solution containing 50 mM Mn^{2+} was added and equilibrated for 10 min, after which the process was repeated two more times. I also grew crystals with only Mn^{2+}. To grow crystals in the presence of Mn^{2+} only (without Mg^{2+} and Ni^{2+}), crystals were grown with 70 mM Mn^{2+}. The crystals possess very similar unit cell dimensions (a=97.3, b=100.46, c=141.63) and have very similar crystal packing although the space group of the native crystal is $P2_12_12_1$ while the space group of the Mn^{2+}-only crystal is $C222_1$. The change of the space group in the absence of Ni^{2+} was also observed with crystals grown in the presence of only Mg^{2+}. The Mn^{2+}-only crystals diffracted at a lower resolution (5.2 Å), but the Mn^{2+} anomalous signal from this crystal was stronger (~6 σ). Both the Mn^{2+}-soaked crystal and the crystal grown in the presence of Mn^{2+} diffracted X-rays to 5.2 Å and 5.7 Å, respectively. A long wavelength (1.50-1.55 Å) was utilized to maximize the anomalous scattering power. Anomalous difference Fourier maps were calculated using the model phase without any metals.

I carried out anomalous scattering studies with native crystals grown in the presence of Mg^{2+} and Ni^{2+}. Since the anomalous scattering power of phosphate is weak and slightly lower than sulfur (f " ~0.5 electrons for phosphate and ~0.65 electrons for sulfur at 1.7Å), I collected a highly redundant dataset (average redundancy ~11) from a relatively well-diffracting native crystal (~4.0 Å). The resulting anomalous difference Fourier map revealed density peaks corresponding to most of the methionine residues as well as phosphates from C_{55}-P at the dimer interface, indicating that the quality of the data is high.

To identify the ions in loop E, I calculated an anomalous difference Fourier map using the 3.3-Å native data that was collected at a short wavelength (0.975 Å) from the crystal grown in the presence of Mg^{2+} and Ni^{2+}.

1.4.2.3 Cross-Linking Experiments

Purified $MraY_{AA}$ in decyl maltoside (DM) was subjected to cross-linking using the membrane-permeable cross-linking reagent disuccinimidyl suberate (DSS) at various concentrations at room temperature (RT). The reaction was quenched after 25 min with the addition of 100 mM Tris buffer and then subjected to gel electrophoresis. The oligomeric status of $MraY_{AA}$ was identified by Coomassie staining. As for the structure-based disulfide bridge experiment, *E. coli* cell membranes were isolated and subjected to cross-linking using the membrane-permeable oxidant copper phenanthroline (200 μM) at RT. The reaction was quenched after 25 min with the addition of 20 mM N-

ethylmaleimide (NEM) and 50 mM EDTA. Protein loading buffer containing SDS was subsequently added to the membranes to a final SDS concentration of 2% (w/w) for solubilization. The oligomeric status of $MraY_{AA}$ was identified by Western blot using anti-His antibodies.

1.4.2.4 Mass Spectrometry

To detect lipids associated with $MraY_{AA}$ in the crystals, crystals were washed with mother liquor without the protein three times and dissolved into water. The solution was sonicated briefly with a water-bath sonicator. Ziqiang Guan performed the mass spectrometry (MS) experiments to identify lipids associated with $MraY_{AA}$. My contribution is to provide purified $MraY_{AA}$ for MS analysis. Lipids that co-purified with $MraY_{AA}$ were extracted by the Bligh-Dyer method and analyzed by LC-MS using a Shimadzu LC system (comprised of a solvent degasser, two LC-10A pumps and a SCL-10A system controller) coupled to a QSTAR XL quadrupole time-of-flight tandem mass spectrometer (AB-Sciex, Foster City, CA). Undecaprenyl phosphate (C_{55}-P) and Lipid I were identified by exact mass measurement and tandem mass spectrometry (MS/MS) experiments that revealed their characteristic fragments.

The assay was performed in a final volume of 100 µl containing 100 mM Tris-HCl, pH 7.5, 40 mM MgCl2, 1.1 mM C_{55}-P, 250 mM NaCl, 0.25 mM UDP-MurNAc pentapeptide and 1 mM n-Dodecyl β-D-maltoside. 0.5µM MraY protein was added to initiate the reaction. The mixture was incubated for 25 min at 37 °C under shaking. The reaction was

quenched with lipid extraction by the Bligh-Dyer method followed by mass spectroscopy experiments.

1.5 Functional Studies Of $MraY_{AA}$

1.5.1 Introduction

To test whether purified recombinant $MraY_{AA}$ is functional, functional characterization of $MraY_{AA}$ is necessary. Dr. Jinshi Zhao and Robert Gillespie of Dr. Pei Zhou's group performed the thin-layer chromatography (TLC)-based translocase assays. The TLC-based translocase assay showed that the recombinant $MraY_{AA}$ is a functional enzyme. Robert Gillespie demonstrated the inhibitory effect of capuramycin on $MraY_{AA}$ with the half maximal inhibitory concentration (IC_{50}) of around 56 μM (± 14.3 μM). My contribution to the TLC-based translocase assays was to provide purified $MraY_{AA}$.

To study the interactions between $MraY_{AA}$ and natural product inhibitors, it is critical to measure equilibrium binding affinities. I have developed a tryptophan fluorescence assay to detect the perturbation of the two conserved tryptophan residues nearby the potential active site by the interactions with inhibitors. Using this assay, I determined the binding affinity of two natural MraY inhibitors, capuramycin and tunicamycin.

These studies showed that $MraY_{AA}$ is functional and inhibited by the natural product inhibitor capuramycin, which makes $MraY_{AA}$ a good model system to study the enzyme from pathogenic bacteria and MraY in general.

1.5.2 Results

1.5.2.1 Purified $MraY_{AA}$ Is Functional

The purified $MraY_{AA}$ in detergent micelles was incubated with UDP-MurNAc-[^{14}C]-pentapeptide and C_{55}-P, and enzyme-mediated Lipid I production was detected by a mobility shift of the radiolabelled pentapeptide. The results show that recombinant $MraY_{AA}$ can catalyze the transfer of phospho-MurNAc-pentapeptide to the carrier lipid C_{55}-P. A negative control experiment using *V. cholerae* concentrative nucleoside transporter (vcCNT) purified with same protocol clearly showed that endogenous *E. coli* MraY does not contribute to the observed activity after purification (Figure 16). We previously determinedthat Ni^{2+} ions are bound in loop E (Figure 6). The translocase assay was also performed in presence of Mg^{2+} (100 mM) and Ni^{2+} (10 mM), which resulted in a fully active enzyme, suggesting that the structure of Ni^{2+}-bound loop E reflects an active conformation (Figure 17).

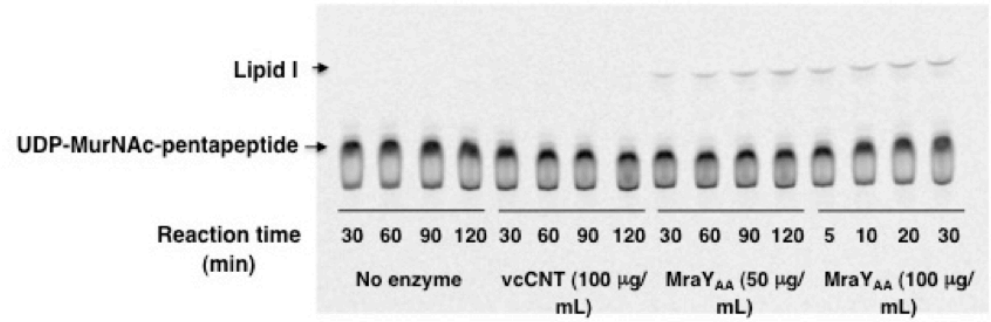

Figure 16: Purified MraY$_{AA}$ Is A Functional Enzyme

Endogenous *E. coli* MraY does not contribute to the observed MraY$_{AA}$ activity. Two control reactions were run in parallel with those of purified MraY$_{AA}$; reactions with no enzyme added (No enzyme) and reactions containing the control membrane transporter molecule ($_{VC}$CNT),expressed and purified using the same methods as MraY$_{AA}$. The control transporter and MraY$_{AA}$ were prepared in parallel.

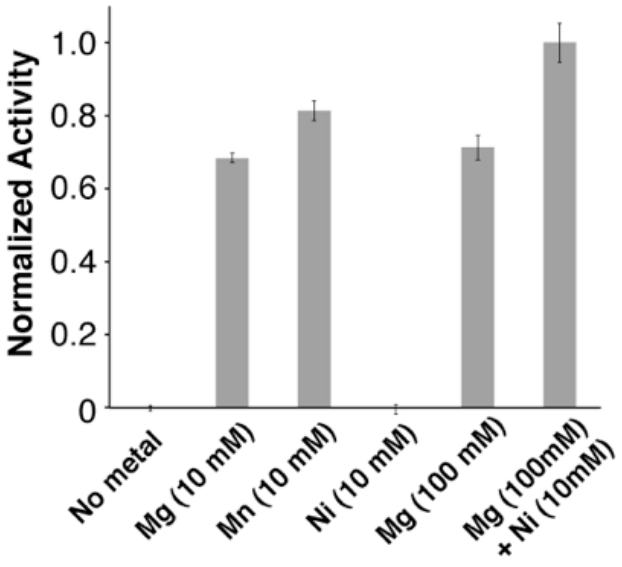

Figure 17: Ni^{2+} Does Not Interfere The Activity Of $MraY_{AA}$

Divalent metal dependence of $MraY_{AA}$ (n=3, SD). The TLC-based translocase assay was performed as described in Materials and Methods

1.5.2.2 $MraY_{AA}$ Is Inhibited By Natural Product Inhibitors

$MraY_{AA}$ contains two tryptophan residues in the conserved intracellular loops near the active site on the basis of sequence and our structure model. The binding of natural inhibitors, including tunicamycin and MraY-specific capuramycin, to $MraY_{AA}$ is characterized by the tryptophan fluorescence assay. Upon titration with either capuramycin or tunicamycin (B complex, Sigma-Aldrich), I consistently observed about 6% decrease in tryptophan (Trp) fluorescence signal. The plot is fitted with a one-site model under the assumption of no co-operativity between the protomers. The dissociation constants (Kd) of capuramycin and tunicamycin are 0.53 ± 0.09 μM and 0.98 ± 0.14 μM respectively (Figure 18).

The translocase assay also showed that $MraY_{AA}$ could be inhibited by the MraY-specific natural product inhibitor capuramycin with an IC_{50} value of 56 ± 14.3 μM (Figure 19)

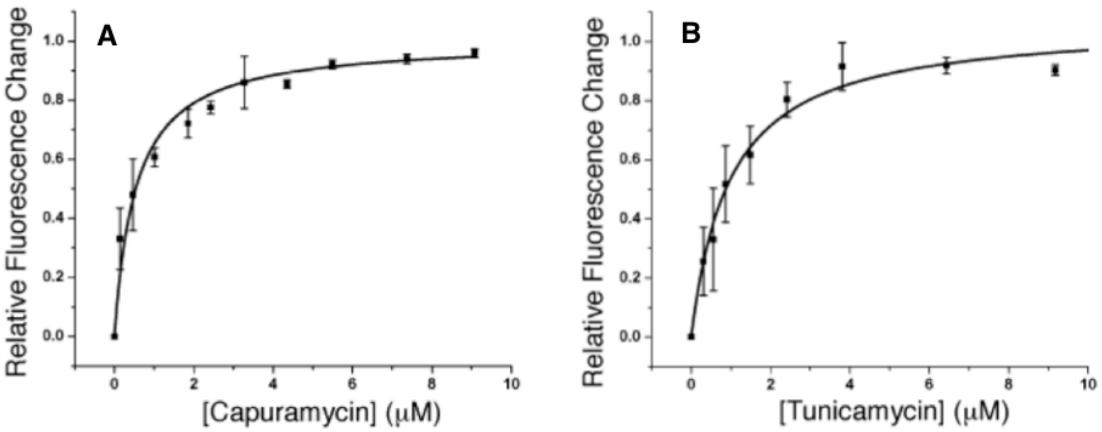

Figure 18: Antibiotics Of Natural Origin Bind To And Inhibit $MraY_{AA}$

Tryptophan fluorescence titration curves of $MraY_{AA}$ upon **(A)** Capuramycin and **(B)** Tunicamycin titration. A one-site binding model was used to fit each of the curves with $K_D = 0.98 \pm 0.14$ μM for Tunicamycin and $K_D = 0.53 \pm 0.09$ μM for capuramycin (n=3, S.D.).

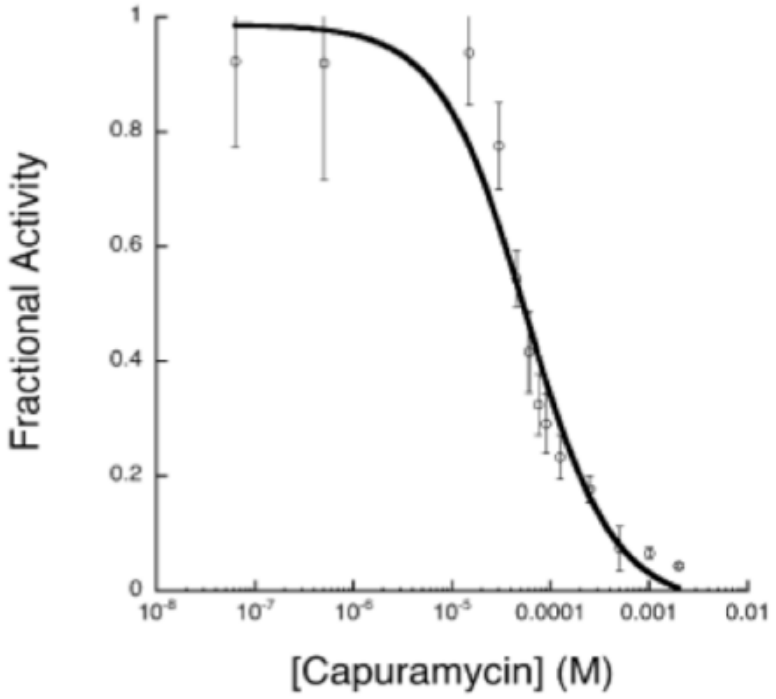

Figure 19: Capuramycin Inhibition Curve Of $MraY_{AA}$

Capuramycin inhibition curve of $MraY_{AA}$ with IC_{50} = 56.4 ± 14.3 μM (N=3, S.D.).

1.5.2.3 Mutations In The $MraY_{AA}$ Active Site And Potential Substrates Binding Site Compromise Catalytic Activity

To further test the functionalities of the catalytic residues (D117, D118 and D265) and three Ni^{2+}-coordinating histidine residues (H324, H325 and H326) in the conserved intracellular loop E (Figure 10B,D), Jinshi Zhao carried out the translocase assays with $MraY_{AA}$ in which these residues were substituted with alanine. We chose I83A as a positive control because I83 is located away from the putative active site. My contribution was to provide mutant enzymes for the translocase assay. Contrary to the positive control mutation I83A that retains full activity, all three catalytic mutations cause a complete loss of function. However, only one histidine mutation on loop E (H324A) abolishes the activity. Two other histidine mutations as H325A and H326A maintain about 35~50% of activity (Figure 20). The proximity of H324 but not H325 or H326 to the active site might be the reason.

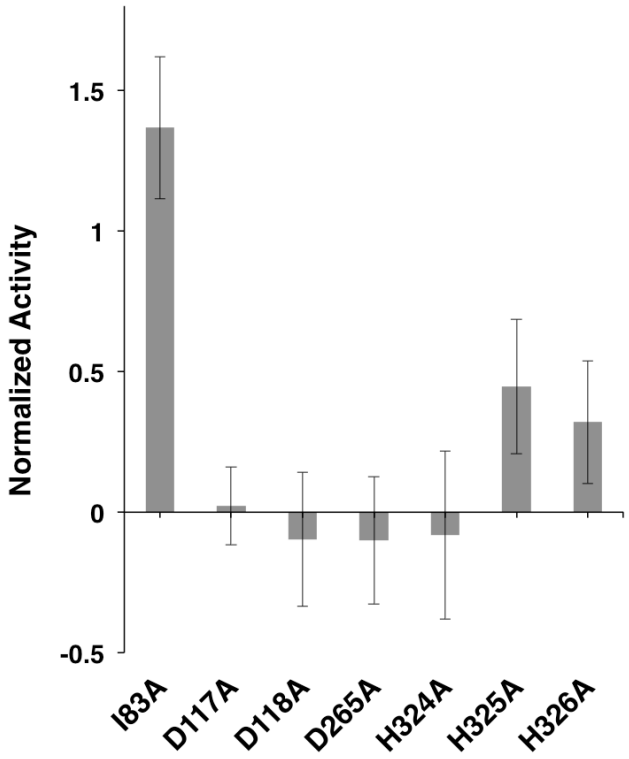

Figure 20: Functional Assay Of $MraY_{AA}$ Mutants

The TLC-based MraY functional assay was performed on various $MraY_{AA}$ mutants and normalized against the result of wild-type $MraY_{AA}$.

1.5.3 Materials And Methods

1.5.3.1 TLC-Based Translocase Assay

The translocase assay, typically 15 µl in volume, was performed in vitro at 30°C in an assay buffer consisting of 100 mM Tris-HCl pH 7.5, 500 mM sodium chloride, 0.25% w/v decylmaltoside, 10 mM $MgCl_2$, 1.1 mM undecaprenyl phosphate, 250 µM (1000 cpm/µl) UDP-MurNAc-[^{14}C]-pentapeptide. Both radiolabeled and non-labeled UDP-MurNAc-pentapeptide were purchased from the synthetic facility at the University of Warwick. The reaction was initiated by the addition of enzyme. At the appropriate time point, the reaction was quenched by spotting a 3 µl aliquot on a silica gel 60 TLC plate. After developing, the plates were dried under a stream of cold air and analyzed via PhosphorImager. The results for the mutants are based on substrate conversion after 20 min of the reaction at 30°C. The capuramycin inhibition assay was performed with the same procedure, except that varying concentrations of capuramycin were pre-incubated with $MraY_{AA}$ for 20 min at 30°C, and the capuramycin-$MraY_{AA}$ mixture was added to the reaction buffer to initiate the reaction.

For metal dependence experiments, apo-$MraY_{AA}$ was formed by incubating purified $MraY_{AA}$ with 2 mM EDTA for 30 min on ice. Apo-$MraY_{AA}$ was then diluted 5-fold into purification buffer containing metals as specified and incubated for an additional 30 min on ice. The reaction was initiated by adding the metal/$MraY_{AA}$ mixture to reaction buffer containing 100 mM Tris-HCl pH 7.5, 500 mM sodium chloride, 0.25% w/v decylmaltoside, 1.1 mM undecaprenyl phosphate, 250 µM (1000 cpm/µl) UDP-MurNAc-

[^{14}C]-pentapeptide, and metal at the indicated concentrations. The results for the capuramycin and the metal-dependence assays were based on a time course (10 to 30 min).

1.5.3.2 Capuramycin Synthesis

Capuramycin was synthesized by Do-Yeon Kwon under the supervision of Jiyong Hong. The procedure used in Capuramycin synthesis was modified from the procedure described by Kurosu et al. (Kurosu, Li, and Crick 2009).

1.5.3.3 Tryptophan Fluorescence Titration

To measure the affinities of capuramycin and tunicamycin for $MraY_{AA}$, 5 μM of purified $MraY_{AA}$ in reaction buffer (150 mM NaCl, 20 mM Tris-HCl pH 8.0, 5 mM decylmaltoside, 2 mM DTT) was titrated with either capuramycin or tunicamycin. The Trp fluorescence was measured using a Cary Eclipse fluorometer with excitation wavelength 287.5 nm and emission wavelength 340 nm. The normalized fluorescence changes were fitted using a one-site binding model.

1.6 Discussion

By solving the crystal structure of an MraY ortholog, a member of the PNPT family, I have begun to understand the structural basis of this enzyme's function. With knowledge of the locations of the two putative substrate-binding sites, we present a hypothetical mechanism of Lipid I generation by MraY (Figure 21). MraY contains a tilted, protruding, and amphipathic transmembrane helix (TM9b) that serves a critical role in the binding of both substrates. First, together with the cytoplasmic loop E, TM9b presents the "lasso"-like binding site for the substrate UDP-MurNAc-pentapeptide. Second, by providing a concave, inverted-U-shaped groove around TM9b, MraY appears to present the binding site for the hydrophobic undecaprenyl group of C_{55}-P. By capturing these two substrates, MraY (and presumably other members of the PNPT family) can position catalytically important groups of substrates effectively into an active site that is located at the inner-leaflet membrane region of the protein.

Our hypothetical mechanism does not distinguish the order of substrate binding. There currently are two mechanistic models: a two-step mechanism that involves an intermediate where the phospho-MurNAc-pentapeptide is covalently linked to the enzyme, and a single-step mechanism that posits that C_{55}-P directly attacks UDP-MurNAc-pentapeptide (Al-Dabbagh et al. 2008; Heydanek, Struve, and Neuhaus 1969). Although our hypothetical mechanism is in line with the single-step, our structure cannot distinguish between the two possibilities, as our positioning of the phosphates from C_{55}-P and UDP-MurNAc-pentapeptide is hypothetical. Further studies will clarify this issue.

It is interesting to point out that only polyisoprenyl phosphates are used as carrier lipids: undecaprenyl phosphate in prokaryotes and dolichol phosphate in eukaryotes. Compared to typical acyl-chain-containing fatty acids, polyisoprenyl phosphates are very long and elastic (de Kruijff, van Dam, and Breukink 2008). One possible reason for the PNPT family using a polyisoprenyl group as a substrate carrier lipid is specific recognition. Since the polyisoprenyl group has a limited degree of rotational freedom due to the double bonds of the isoprenyl units, it can make many pseudo-helical turns and bends in the membrane (de Kruijff, van Dam, and Breukink 2008). We hypothesize that the inverted-U-shaped groove around TM9b creates a specific binding site for the undecaprenyl group. Consistent with our hypothesis, studies have shown that two members of the PNPT family, WecA and eukaryotic GPT, are highly specific for their lipid substrates despite the only difference being the presence of a saturated α-isoprene unit ([C_{55}]dolichol-P) versus an unsaturated α-isoprene unit (C_{55}-P) (Rush, Rick, and Waechter 1997). Another interesting hypothesis for why polyisoprenyl phosphates are used as carrier lipids is their elastic properties. Once the sugar is attached to the lipid carrier, the polyisoprenyl phosphate must be flipped to the periplasmic side of the membrane, and the lipid's elastic properties may facilitate the flippase-mediated flipping procedure.

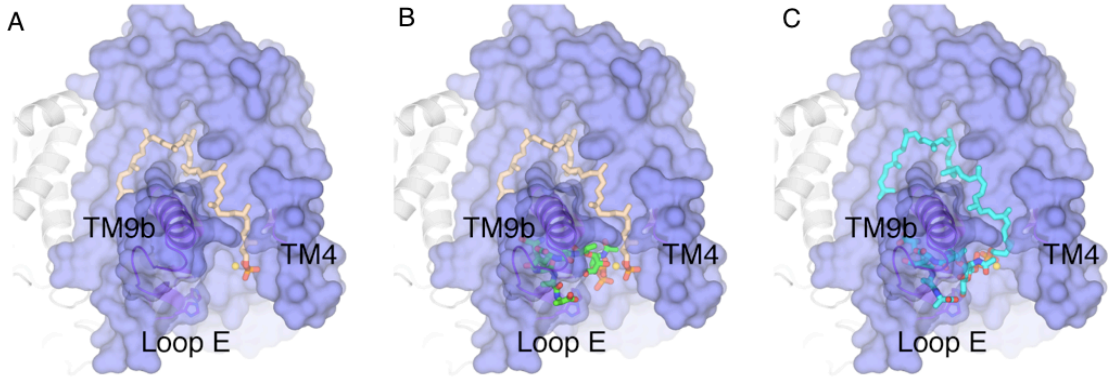

Figure 21: A Hypothetical Mechanism Of Lipid I Generation By MraY.

(A) C_{55}-P bound to MraY. C_{55}-P is shown in stick representation with the undecaprenyl group colored in yellow and the phosphate colored in red. The yellow sphere is Mg^{2+}. **(B)** UDP-MurNAc-pentapeptide and C_{55}-P bound to MraY. The uridine portion was omitted from the hypothetical model. MurNAc-pentapeptide is colored in green with diphosphates colored in red. **(C)** Lipid I (cyan) bound to MraY.

1.7 Future Directions

1.7.1 Crystal Structures With Substrates, Products Or Inhibitors

Based on the unbiased electron density (2Fo-Fc and Fo-Fc OMIT) surrounding TM9b and Loop E, I hypothesized that C_{55}-P binds to the groove around TM9b and UDP-MurNAc-pentapeptide to the space between TM9B and loop E. However, this is not conclusive with the current low-resolution structure and the possible heterogeneity of the substrates or product binding in the crystal. The functional assay showed the inhibitory effect of capuramycin and tunicamycin on $MraY_{AA}$. However, my current structure cannot explain the mechanism by which these molecules act to inhibit MraYAA.

Therefore, after solving the structure of apo-MraY, the next step is to understand the catalytic mechanism of MraY and how natural product inhibitors inhibit MraY function. A series of snapshot structures of MraY in complex with substrates, product or inhibitor should be the next step in elucidating the structure-function relationship of this enzyme. By further optimizing the crystallization conditions or employing different crystallization methods (such as lipid cubic phase, co-crystallization with a monoclonal antibody), we will be able to obtain high-resolution structures, which will show the details of substrate or product binding by the enzyme. Co-crystallizing or soaking with substrates (C_{55}-P and UDP-MurNAc-pentapeptide), product (Lipid I) and inhibitors (Capuramycin and Tunicamycin) are the future directions for MraY crystallization.

2 Structural Studies Of The Ternary Complex Of Na_V C-Terminal Domain (CTD, Fibroblast Growth Factor Homologous Factor (FHF) And Calmodulin

2.1 Summary

Voltage-gated Na^+ (Na_V) channels initiate action potentials in excitable cells such as neurons and cardiomyocytes. Na_V channels are composed of a transmembrane domain responsible for voltage-dependent Na^+ conduction and a cytosolic C-terminal domain (CTD) for channel regulation through interactions with several auxiliary proteins including fibroblast growth factor homologous factors (FHFs) and calmodulin (CaM). Through the collaboration between our lab and Geoffrey Pitt's lab, we have studied the mechanism of Na_V channel regulation by auxiliary protein using X-ray crystallography, biochemistry, and electrophysiology. My contribution to the project is structure determination of the ternary complex structure of Na_VCTD/CaM/FHF with and without calcium ion using X-ray crystallography.

The ternary complex structure in the absence of calcium was solved at 2.2-Å resolution with the combination of Na_V1.5CTD/CaM/FHF2B. Voltage-gated sodium channel 1.5 (Na_V1.5) is the major sodium channel expressed in heart tissue. Clinical studies link a variety of mutations on the C-terminus of Na_V1.5 with arrhythmogenic heart diseases such as long QT syndrome and Brugada syndrome. The calcium-free complex structure showed the calcium-independent binding of calmodulin to the IQ motif of Na_V1.5CTD. Interactions between Na_V1.5CTD and FHF2B are also observed in this structure. Several disease-causing mutations of Na_V1.5CTD are found within the regions interacting with FHF2B and calmodulin. A critical interaction between Na_V1.5CTD and FHF2B that

contributes to FHF-subtype specificity is also identified from our structural and functional studies.

In this project Chaojung Wang cloned, expressed and crystallized the ternary complex. She also carried out the ITC binding assay. Haidun Yan performed the electrophysiology experiments. I froze crystals, collected diffraction data, solved and refined all of the complex structures described here.

2.2 Introduction

2.2.1 Voltage-Gated Sodium Channel

A large and rapid influx of sodium ions (I_{Na}) through voltage-gated Na^+ (Na_V) channels is responsible for the rapid upstroke of the action potential in the axon initial segment of neurons. Dysregulation of Na_V channels leads to a variety of neurological disorders. Mutations in SCN1A and SCN2A, which encode $Na_V1.1$ and $Na_V1.2$, respectively, lead to various epilepsy syndromes. Gain- and loss-of-function mutations have both been reported (Meisler, O'Brien, and Sharkey 2010), highlighting the importance of the precise regulation of channel function. Mutations in the SCN5A-encoded cardiac $Na_V1.5$, with similar peptide consequences, have been linked to various inherited arrhythmias (Zimmer and Surber 2008). Na_V channels, which are monomers with tetrameric repeats of six transmembrane (TM) segments, share a similar architecture with other voltage-gated cation (Ca^{2+} and K^+) channels. In these six TM segments, the first four TM segments (S1–S4) comprise the voltage-sensor domain (VSD) and the last two TM segments (S5 and S6) make up a central pore when assembled as a tetrameric configuration. The pore mediates selective cation permeation through its selectivity filter, and this conduction can be allowed (open) or obstructed (closed) by a "gate" near the intracellular membrane surface of the pore lined by S6. In voltage-gated cation channels, VSDs control pore gating upon sensing a change in membrane voltage. Four VSDs are located on the periphery of the central pore (Figure 22).

Although the pore-forming α-subunit is responsible for the fundamental properties of voltage-dependent Na^+ conduction, auxiliary proteins regulate channel function. Most voltage-gated ion channel structural studies have focused on the general mechanisms of permeation and voltage-dependent gating by studying prototypical K_V channels, such as an archaeal K_V channel (K_VAP), the Shaker-type K_V channel (K_V1.2), and the Na_V channel from *Arcobacter butzleri* (Na_VAb) (Jiang et al. 2003; Lee et al. 2005; Long, Campbell, and MacKinnon 2005; Payandeh et al. 2011). Much less is known about how their intracellular domains, such as the Na_V cytoplasmic C-terminal domain (CTD), modulate channel function. However, most Na_V channel auxiliary proteins interact with the cytoplasmic C-terminal domain (CTD) of the channel's α-subunit (Figure 22). Among these are the Na_V β subunit through its short cytoplasmic domain (Spampanato et al. 2004), calmodulin (Mori et al. 2003), and members of the fibroblast growth factor homologous factor (FHF) family (Liu Cj, Dib-Hajj, and Waxman 2001). Not only is the Na_V CTD important for the regulation of channel activity, but a significant number of disease causing mutations are localized to Na_V CTDs (Lossin 2009; Ohmori et al. 2006; Spampanato et al. 2004) and their associated proteins (van Swieten et al. 2003).

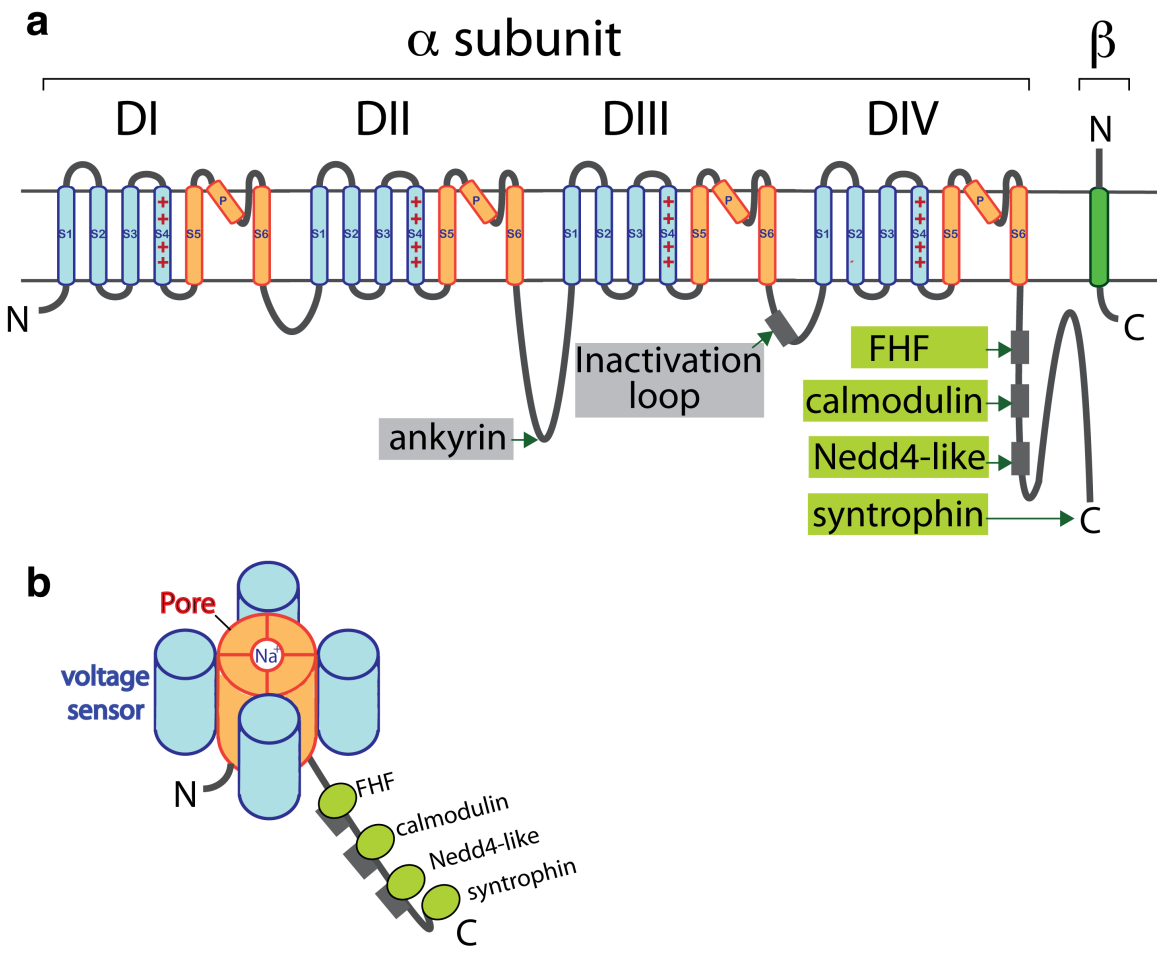

Figure 22: The Architecture Of Voltage-Gated Na^+ Channels

(A). Overall architecture of a voltage-gated Na^+ channel and its auxiliary proteins. The Na_V pore-forming α-subunit is a monomer with tetrameric repeats of 6 transmembrane (TM) segments. Each repeat consists of a voltage-sensor domain (first 4 TM helices, cyan) and a pore domain (last 2 TM helices, orange). Arginines on S4 that are important for voltage sensing are indicated with red plus signs. Auxiliary proteins that interact with the C-terminal domain (CTD) are shown (green). The most structured region (1773-1940) of the CTD that was used for crystallization includes binding sites for FHF and

calmodulin. (B). A tetrameric pore (orange) is located centrally while 4 voltage-sensors (cyan) are located peripheral to the central pore.

2.2.2 Fibroblast Growth Factor Homologous Factor (FHF)

Fibroblast growth factor homologous factors (FHFs) belong to the fibroblast growth factor (FGF) superfamily (Smallwood et al. 1996), but are functionally different from canonical FGFs (Olsen et al. 2003). The four FHF genes (FGF11–FGF14) encode ten isoforms generated by alternative splicing of exons that encode an extended N-terminus preceding a core domain that is homologous with FGFs. Unlike FGFs, FHFs don't have the exporting signal sequences at their N-termini and so are not secreted from cells (Smallwood et al. 1996). Furthermore, they cannot activate FGF receptors due to minor differences in their FGF-like core structure (Olsen et al. 2003). Instead of serving as extracellular growth factors, FHFs bind to Na_V CTDs and modulate Na_V channel function from the cytoplasm (Liu Cj, Dib-Hajj, and Waxman 2001). The modulating role of FHFs on Na_V function was highlighted by the finding of FGF14 as the locus for spinocerebellar ataxia 27 (van Swieten et al. 2003) and demonstration that the FGF14 mutant reduces Na_V channel currents, alters channel gating, and decreases neuronal excitability in a dominant negative manner (Laezza et al. 2007). Although several FHFs are expressed in the brain, they are not functionally redundant. FGF14 knockout mice show ataxia, dyskinesia, and dystonia (Q. Wang et al. 2002). Knockout of FGF12 exacerbates all of those phenotypes and exaggerates the effects on neuronal Na_V channels (Goldfarb et al. 2007). In addition to regulating Na^+ conduction, FHFs also affect Na_V channel trafficking to the plasma membrane and targeting to the axon initial segment (Laezza et al. 2007; C. Wang, Wang, et al. 2011).

2.2.3 Calmodulin Acts As A Calcium Sensor For Ca^{2+}-Dependent Na_v Regulation

The ubiquitous Ca^{2+} sensor calmodulin (CaM) binds Na_V CTDs, near the putative FHF interaction site. A familial-autism-associated mutation localizes to the CaM binding region in $Na_V1.2$ and is hypothesized to alter the regulation of Ca^{2+}-dependent $Na_V1.2$ channel function (Weiss et al. 2003). How CaM controls Na_V channel function is still unknown, and whether Ca^{2+} also affects Na_V channel function through direct binding to a putative EF hand in the CTD has been controversial (Miloushev et al. 2009; Shah et al. 2006).

2.3 Structure Determination Of The Ternary Complex Without Calcium

2.3.1 Results

2.3.1.1 Structure Of An Na_v CTD In Complex With FHF And CaM

We chose the $Na_V1.5$ CTD and FHF2B because the resulting ternary complex was biochemically stable and yielded well-diffracting crystals among the several different combinations of Na_V CTDs and FHFs tested. The sequence of the Na_V CTD is highly conserved among the subtypes (over 75% identical between $Na_V1.5$, $Na_V1.1$, and $Na_V1.2$), and the solution structures of the EF-hand fragments of the $Na_V1.2$ CTD and $Na_V1.5$ CTD are nearly identical (Chagot et al. 2009; Miloushev et al. 2009). We postulated that failed previous attempts to crystallize an Na_V CTD in complex with an FHF (Goetz et al. 2009) might be due to the lack of inclusion of CaM and consequent nonspecific interactions in the complexes because we observed by size-exclusion chromatography an apparent higher order (stoichiometry > 1:1, $Na_V1.5$ CTD:FGF13) binary complex that was reduced by addition of CaM. The ternary complex was stable. Its elution volume on the size exclusion column was consistent with a molecular weight about equal to the sum of its individual components (60 kDa), indicating the stoichiometry of the ternary complex is 1:1:1 (Figure 23).

The resultant ternary complex was crystallized in the space group $P2_13$ (a = b = c = 126.04 Å) with one copy of the ternary complex in each asymmetric unit. The crystals

were grown in the presence of 5 mM EGTA and diffracted to 2.2-Å Bragg spacings. The experimental phases were derived by single anomalous dispersion from selenomethionine-substituted crystals. The final model contains the $Na_V1.5$ CTD amino acids 1776–1928; FGF13U amino acids 11–158 (because the N-terminal "U" extension that defines this isoform is not present in the model, it is hereafter designated "FGF13"); and the entire CaM except for the N-terminal four amino acids and the loops from residues 22–27 and 57–61 in the N-lobe. The model refined to an R_{free} value of about 22.7% (Table 3).

Figure 24 shows the overall architecture of the ternary complex. The Na_V CTD is composed of one globular domain (α1– α5) followed by an extended 29-amino acid helix (α6) that contains the CaM-binding IQ motif in its proximal portion. FGF13 binds to the globular domain of the CTD. The five α helices in the globular domain of the Na_V CTD are separated by four short anti-parallel β strands. The first four helices (α1– α4) with two β strands (β1 and β3) adopt a paired EF-hand fold, as was observed in NMR structures of Na_V CTD fragments containing only α1– α4 (root-mean-square deviation [r.m.s.d] of 0.62 Å; Figure 25) (Chagot et al. 2009; Miloushev et al. 2009). Addition of α5 plus a loop between α5 and α6 and a short β strand (β4) to the paired EF-hand fold creates the binding site for FGF13 (Figure 24C). The presence of β4 turns the loop between α3 and β3 into a short β strand (β2) that forms a short β sheet with the rest of the β strands (β1–β4) (Figure 24C).

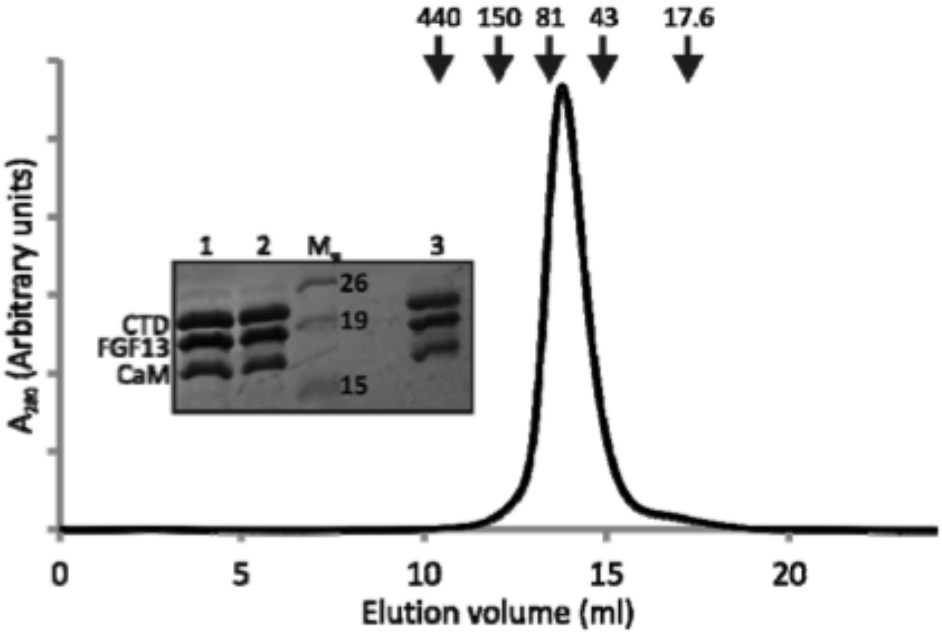

Figure 23. Gel Filtration Chromatography Profile Of The Ternary Complex Of $Na_v1.5$ CTD, FGF13U, And CaM.

The purified complex was run on a Superdex 200 hr 10 / 30 gel filtration column (GE life sciences). Migration of standards (Ferritin, mw 440 kDa; human IgG, mw 150 kDa; human transferrin, mw 81 kDa; ovalbumin, mw 43 kDa; and myoglobin, mw 17.6 kDa) is indicated by arrows. The inset shows samples from the peak (lanes 1 and 2) used for crystallization and from a resultant crystal after solubilization in SDS loading buffer (lane 3). The molecular weight markers are indicated.

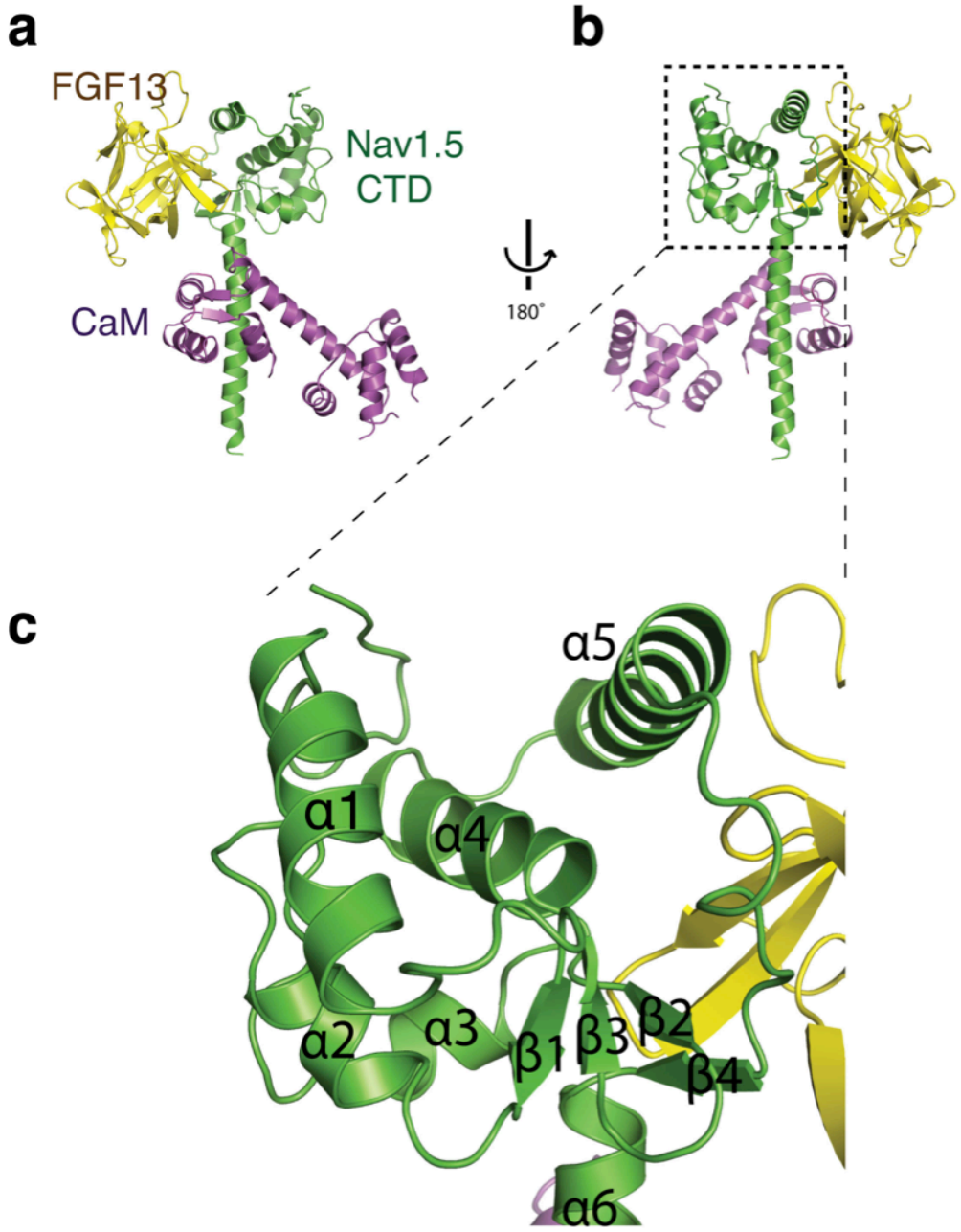

Figure 24: Overall Architecture Of The Ternary Complex Of $Na_v1.5$ CTD, FGF13, And CaM.

Structure of $Na_V1.5$ CTD (green) in complex with FGF13 (yellow) and CaM (magenta). (b) Same as (a) but rotated 180°. (c) Zoomed-in view of $Na_V1.5$ CTD with the same orientation as (b). Secondary structural elements are labeled accordingly.

Table 4: Data Collection, Phasing And Refinement Statistics

	Native	**SeMet derivative**
Data collection		
Space group	$P2_13$	$P2_13$
Cell dimensions		
***a, b, c* (Å)**	126.04, 126.04, 126.04	125.57, 125.57, 125.57
α, β, γ (°)	90, 90, 90	90, 90, 90
		Peak
Wavelength (Å)	1	0.97936
Resolution (Å)	50-2.2 (2.24-2.2)*	50-2.91 (2.96-2.91)
***R*sym or *R*merge (%)**	6.7 (36.0)	10.4 (51.4)
I/σI	36.9 (2.1)	47.88 (5.0)
Completeness (%)	99.8 (87.4)	100 (100)
Redundancy	8.2 (3.0)	17.6 (13.8)
Refinement		
Resolution (Å)	2.2	
No. reflections	34027	
R_{work}/ R_{free} (%)	21.0/22.7	
No. atoms		
Protein	3488	
Mg^{2+}	3	
Water	202	
B-factors (Å2)		
Protein	51.58	
Mg^{2+}	44.03	
Water	51.33	
R.m.s.d		
Bond lengths (Å)	0.011	
Bond angles (°)	0.823	

*Highest resolution shell is shown in parenthesis.

Figure 25: Superposition Of The NMR Structure Of $Na_v1.5$ CTD Fragment (A1-A4) With The Crystal Structure Of $Na_v1.5$ CTD From The Ternary Complex.

The NMR structure (PDB ID: 2KBI) is colored red. $Na_v1.5$ CTD (A1-A6), FGF13, and CaM are colored green, yellow, and magenta, respectively.

2.3.1.2 Interaction Between Na_v CTD And FHF

Initial analysis of the interaction surface between the Na_V CTD and FGF13 provides a means to understand functional consequences of disease-causing mutations in Na_V CTDs, but yields little initial insight into the specificity of CTD-FHF pairwise interactions and functional consequences. The shape of the Na_V CTD-FGF13 binding surface has a relatively high shape complementary index of ~0.67 (Lawrence and Colman 1993). The buried surface area is ~2,350 Å. The FGF13-binding surface on the Na_V CTD is dominated by a depression formed by α4 and sequential segments starting with the carboxy-terminal segment of α5, the subsequent extended loop, β4, and the beginning of α6 (amino acids Phe1879 to Arg1898) (Figure 24C and Figure 26B). The Na_V CTD binding surface on FGF13, highly conserved among the other FHF family members, contains several knob-like structures that fit into the Na_V CTD depression (Figure 26C,E). The main anchor appears to be a knob formed by the side chains of Leu56 and Arg57 on FGF13 that protrudes into the Na_V CTD to interact with His1849 and Asp1852 of α4 (Figure 26C). A second protrusion on FGF13 (Asn97) fits into a crevice on the Na_V CTD formed between Asp1839 and Pro1841. The involvement of these interacting residues is underscored by disease-associated mutations (Figure 27). For example, epilepsy-associated mutations in $Na_V1.1$, D1866Y (Spampanato et al. 2004) and T1909I (Ohmori et al. 2006), reside in residues (Asp1852 and Thr1895 in the $Na_V1.5$ CTD, respectively) that form contacts with FGF13 (Figure 26). Additionally, D1839G in $Na_V1.5$, which accepts the knob formed by Asn97 on FGF13, has been associated with

the fatal cardiac arrhythmia long QT syndrome (Benhorin et al. 1998). Because the key residues that form the FGF13 binding surface are conserved among the other Na_V CTDs and the critical residues forming the complementary Na_V CTD binding surface on FGF13 are conserved among the other FHFs, this interaction motif is likely conserved among other Na_V CTD-FHF pairs. How is the specificity encoded between specific Na_Vs and FHFs? The variable FHF N-termini may contribute, but it cannot explain why FGF12B (that essentially lacks the extended N-terminus found in all other FHF isoforms) can bind to and modulate $Na_V1.5$ but not $Na_V1.1$, as previous studies showed (C. Wang, Hennessey, et al. 2011). Comparison of the determinants for FGF13 binding in $Na_V1.5$ with the homologous amino acids in the $Na_V1.1$ CTD identified one difference: Glu1890, which interacts with Lys14 of FGF13 by a salt bridge (Figure 26C, highlighted in red, and Figure 28A), is replaced by a glutamine (Gln1904) at the homologous position in $Na_V1.1$. We speculated that the loss of the salt bridge with Lys9 (homologous to Lys14 in FGF13) contributes to the reduced affinity observed between FGF12B and $Na_V1.1$. To test this hypothesis we performed a charge reversal swap between Lys9 in FGF12B and Glu1890 in $Na_V1.5$ and analyzed the effects on binding affinity between the $Na_V1.5$ CTD and FGF12B using isothermal titration calorimetry. Mutating either Lys9 in FGF12B to Glu ($FGF12B^{K9E}$) or Glu1890 in $Na_V1.5$ to Lys ($Na_v1.5\ CTD^{E1890K}$) reduced binding affinity by at least 20-fold (Figure 28C and Table 5). However, the when both $Na_V1.5$ and FGF12B were mutated the affinity was restored to the level seen with the wild-type pair. Because we have equilibrium binding data for the wild-type and charge-reversed mutants of $Na_v1.5$ and FGF13, we performed a thermodynamic double mutant cycle

analysis to measure the degree of energetic coupling between these sites. The resulting energetic coupling constant for the salt bridge interaction is ~1100 (~4 kcal/mol). This high value (>5 is considered significant) suggests that the salt bridge interaction is energetically significant and formed by charged-hydrogen bonding (Hidalgo and MacKinnon 1995). Consistent with these results, FGF12B^{K9E} co-purified with $Na_V1.5$ CTD^{E1890K}, like the wild-type pair, when coexpressed in *E. coli*. Neither FGF12B^{K9E} nor $Na_V1.5$ CTD^{E1890K} co-purified with the wild-type binding partner (Figure 28D). The consequences upon channel function were consistent with the binding data. As previously shown, FGF12B induced a depolarizing shift in the $V_{1/2}$ of steady-state inactivation of $Na_V1.5$ currents (C. Wang, Hennessey, et al. 2011). In contrast, the FGF12B^{K9E} mutant did not modulate steady-state inactivation, nor was steady-state inactivation of $Na_V1.5^{E1890}$K modulated by wild-type FGF12B (Figure 28F and Table 5). This lack of modulation was not due to decreased expression of either the mutant FHF or Na_V (Figure 29), so it likely reflects the absence of interactions with the coexpressed partner. In contrast, FGF12B^{K9E} induced a depolarizing shift in steady-state inactivation for $Na_V1.5^{E1890K}$ that was similar to the shift induced by wild-type FGF12B for wild-type $Na_V1.5$. To test whether the absence of the salt bridge between $Na_V1.1$ and FGF12B accounts for the fact that FGF12B cannot modulate $Na_V1.1$, we then measured the affinities by ITC between FGF12B and wild-type $Na_V1.1$ CTD or $Na_V1.1$ CTD^{Q1904E}. As previously observed with surface plasmon resonance data (C. Wang, Wang, et al. 2011), the affinity between FGF12B and $Na_V1.1$ CTD is very low. The affinity between FGF12B and $Na_V1.1$ CTD^{Q1904E}, was markedly higher by at least 10-fold, albeit not as

high as between FGF12B wild-type and $Na_V1.5$ CTD (Table 5). Thus, these data support the hypothesis that binding and function is influenced by the salt bridge between the FHF Lys and the Na_V CTD Glu, and this interaction is an important determinant for specificity, while also pointing to the existence of other important interactions not yet identified.

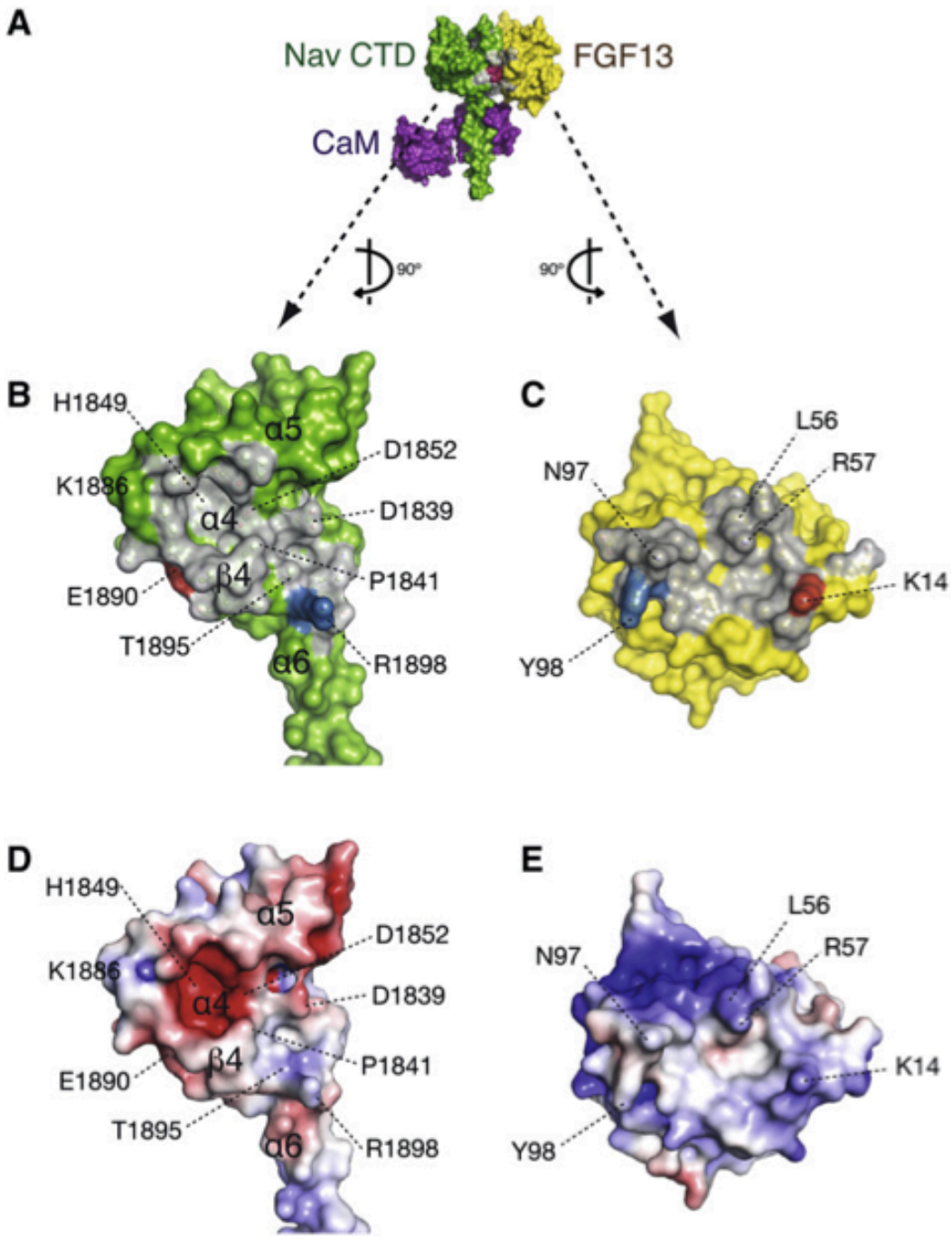

Figure 26: Interactions Between Na_V CTD And FGF13

Surface representation of the ternary complex of the Na_V CTD (green), FGF13 (yellow), and CaM (magenta). The interaction surfaces between the $Na_V1.5$ CTD and FGF13

(within 4 Å) are colored gray. An electrostatic interaction that may be important is shown in red. (**B and C**) The FGF13-interacting surface on the $Na_V1.5$ CTD and the $Na_V1.5$ CTD-interacting surface on FGF13, respectively. In each case, the highlighted molecule is rotated 90^o from **(A)**. Two electrostatic interacting pairs that may be important are shown in red (E1890 in $Na_V1.5$ CTD and K14 in FGF13) and blue (R1898 in $Na_V1.5$ CTD and Y98 in FGF13), respectively. (**D and E**) The electrostatic potential surface representations of **(B)** and **(C)**, respectively. The potential was calculated from 5 kT (negatively charged amino acids) to 5 kT (positively charged amino acids) using the program Adaptive Poisson-Boltzmann Solver (APBS) (Baker et al. 2001).

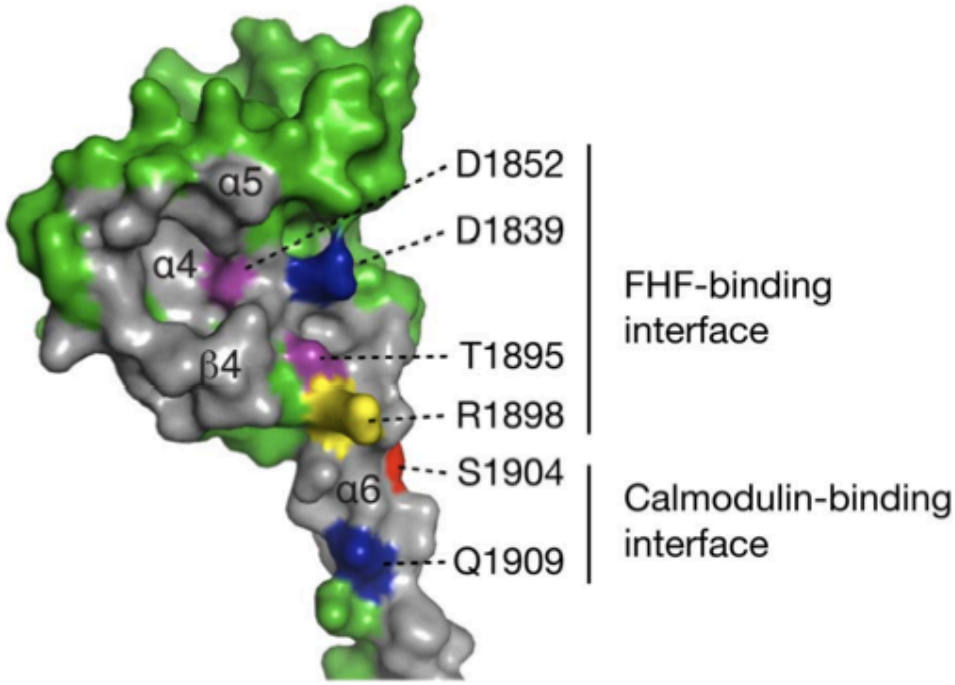

	Mutation	Corresponding residues in Nav1.5
LQT3	Nav1.5 Q1909,D1839	Q1909,D1839
Epilepsy	Nav1.1 D1866,T1909	D1852,T1895
Brugada	Nav1.5 S1904	S1904
Autism	Nav1.2 R1902	R1898

Figure 27: Mapping Disease-Associated Mutations On The $Na_v1.5$ CTD At The Interfaces For FHF And Calmodulin

The sttructure of $Na_V1.5$ CTD is displayed as a surface representation. Mutations correlated to various diseases are annotated with color: blue (LQT3), purple (epilepsy), red (Brugada syndrome), yellow (autism). All mutations are in the surface area interacting with FHF and calmodulin (gray color).

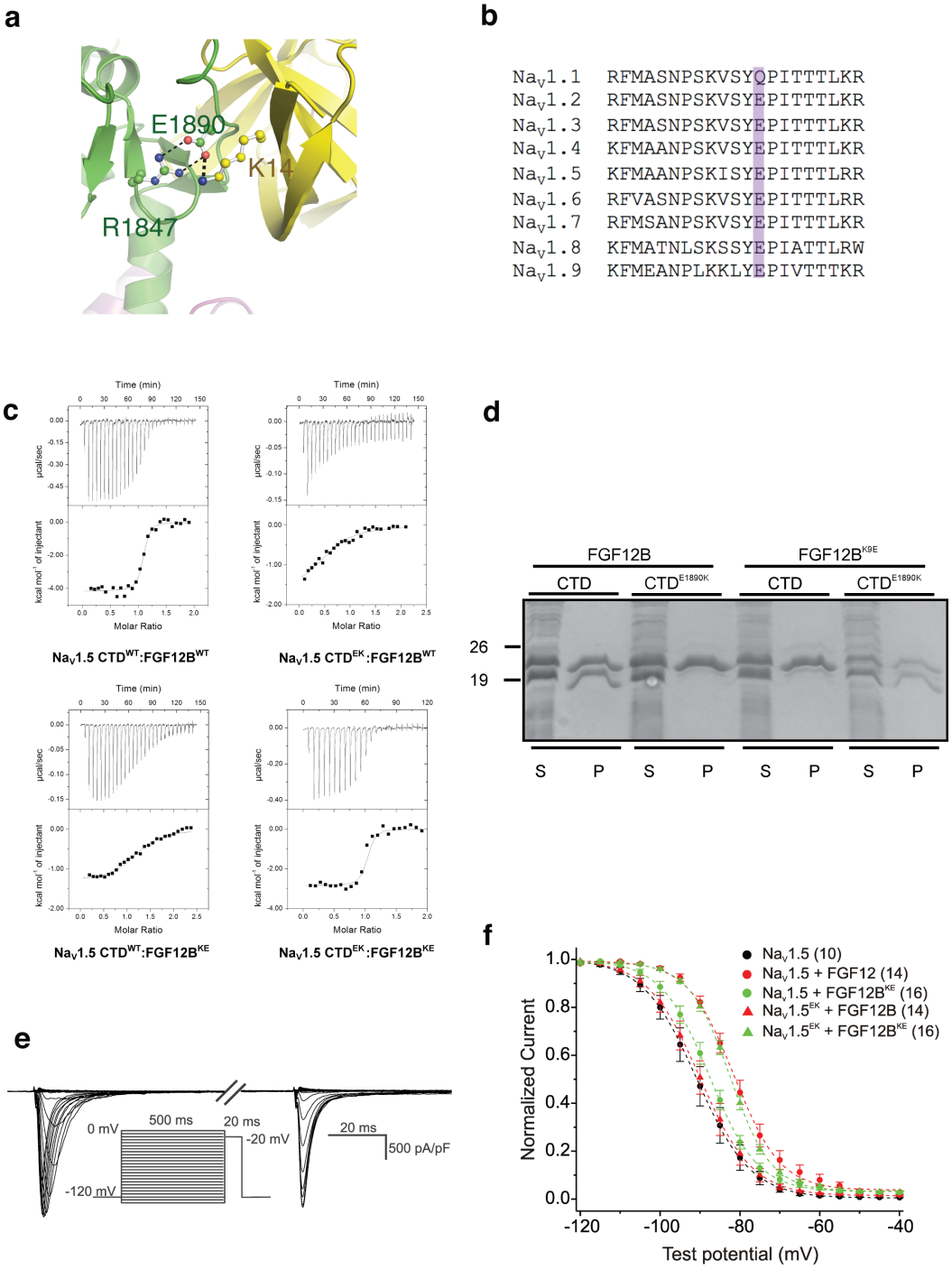

Figure 28: Specificity Between The Na$_v$1.5 CTD And FGF13

(A) Electrostatic interaction between $Na_V1.5$ CTD^{E1890} and $FGF13^{K14}$. **(B)** Sequence alignment among Na_V isoforms shows that Glu 1890 in $Na_V1.5$ is conserved among other isoforms except $Na_V1.1$. **(C)** Sample isothermal titration calorimetry curves of FGF12B binding to $Na_v1.5$ CTD. The total heat exchanged during each injection is fit to a binding isotherm with n, K_D, and ΔHo as independent parameters. $K_D = 0.123 \pm 0.002$ μM, n = 1, and ΔHo = 4,835 ± 235 cal/mol for $Na_V1.5$WT and FGF12B WT. $K_D = 2.37 \pm 0.34$ μM, n = 1.22 and ΔHo = 1,244 ± 181 cal/mol for $Na_V1.5$WT and $FGF12B^{K9E}$. $K_D = 5.04 \pm 0.69$ μM, n = 0.62, and ΔHo = 1,001 ± 312 cal/mol for $Na_V1.5^{E1890}$K and FGF12BWT. $K_D = 0.088 \pm 0.025$ μM, n = 0.98, and ΔHo = 2,746 ± 202 cal/mol for $Na_V1.5^{E1890K}$ and $FGF12B^{K9E}$. Results are means ± SEM with n = 3. **(D)** Coexpression and copurification experiment of wild-type and mutant $Na_V1.5$ CTD and FGF12B shows restoration of interaction with a charge swap.

Table 5: Contribution of Salt Bridge Between FGF12B and $Na_V1.5$ To Binding Affinity And Steady State Inactivation

Na_V	FGF12B	K_d(μM)	$V_{1/2}$ (Steady State Inactivation
$Na_V1.5^{WT}$	-	-	-90.7 ± 2.0*
$Na_V1.5^{WT}$	WT	0.12 ± 0.002	-80.5 ± 1.3
$Na_V1.5^{WT}$	K9E	2.4 ± 0.34*	-87.7 ± 1.1*
$Na_V1.5^{E1890K}$	WT	5.0 ± 0.69*	-89.8 ± 1.8*
$Na_V1.5^{E1890K}$	K9E	0.09 ± 0.025	-82.3 ± 0.7
$Na_V1.1^{WT}$	WT	42.4 ± 12.5	ND
$Na_V1.1^{Q1904E}$	WT	3.7 ± 1.4*	ND

ND, not determined

*: $p < 0.05$ compared to WT-WT. Mean ± SEM with n = 3 for K_D and 10-16 for $V_{1/2}$

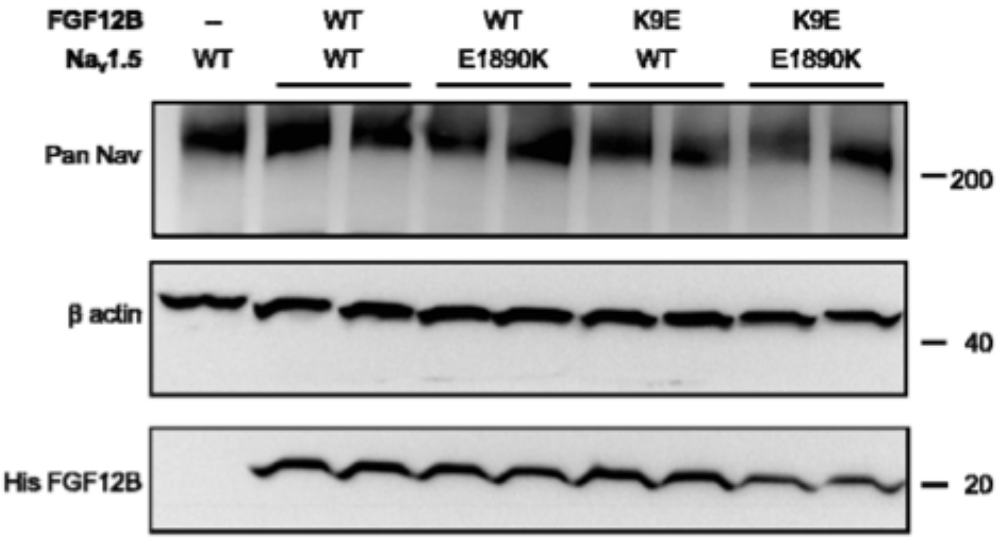

Figure 29: Western Blot Of Cells Expressing Na_v Channels And FGF12B

Immunoblot of lysates from HEK293T cells transfected with $Na_v1.5$, with and without FGF12B, for electrophysiology. Experiments were performed on two separate transfections for each of the combinations of $Na_V1.5$ (wild type or mutant) and FGF12B (wild type or mutant) used in the electrophysiology experiments. Mutation in either $Na_V1.5$ or in FGF12B did not affect the overall amount of protein expressed. α-actin was used as a control for protein loading.

2.3.1.3 Interaction Between Na_v CTD And Calmodulin

The interactions between CaM and the Na_V CTD are mostly localized to the C-lobe of CaM and the IQ-motif in α6 (Figure 30A). The CaM C-lobe adopts a semi-open conformation as observed in NMR structures of apo-CaM bound to a ~20 amino acid Na_V IQ-motif-containing peptide (Chagot and Chazin 2011; Feldkamp, Yu, and Shea 2011)(r.m.s.d. = 1.0 Å for the CaM C-lobe with IQ motif-containing peptide). The CaM C-lobe buries the side chains of Ile1908 and Gln1909 of the Na_V CTD's IQ motif, and also contacts the side chains of Ser1904, Ala1905, and Phe1912 in α6 (Figure 30A). The importance of these observed interactions is underscored by the epilepsy mutation I1922T in $Na_V1.1$ (homologous to Ile1908) (Harkin et al. 2007); and $Na_V1.5$ mutations S1904L (associated with the life-threatening cardiac arrhythmias Brugada Syndrome (Kapplinger et al. 2010) and Long QT Syndrome (Bankston et al. 2007) and Q1909R (associated with Long QT Syndrome (Tester et al. 2005)) (Figure 27).

The linker between the N-lobe and C-lobe of CaM adopts a helical structure (Figure 24). In the NMR structure of CaM bound to the short IQ motif peptide, the linker is disordered (Chagot and Chazin 2011), a discrepancy that is likely because our crystal structure includes a much bigger portion of the Na_V CTD or because the crystal structure captured one of many conformational states of the CaM linker in the ternary complex. The structure of the CaM N-lobe in the ternary complex can be superimposed on the N-lobe of the crystal structure of apo-CaM with an r.m.s.d of ~0.8 Å (Schumacher, Crum,

and Miller 2004) or the N-lobe in the NMR structure of apo-CaM associated with the Na_V CTD IQ motif peptide with an r.m.s.d of ~1.1 Å (Chagot and Chazin 2011).

Even though we grew our crystals in the presence of 5 mM EGTA, we observed two electron density peaks in both Ca^{2+}- binding pockets of the CaM C-lobe. We suspected that the observed peaks were from Mg^{2+}, not Ca^{2+}, because the crystallization solution contained 100 mM Mg^{2+}. To identify the ions in the Ca^{2+}-binding pockets, I performed anomalous diffraction studies on native crystals collected at a long wavelength (1.54 Å). At this wavelength, the anomalous scattering power of Ca^{2+} (~1.1e) is higher than that of sulfur (~0.6e) and much higher than that of Mg^{2+} (~0.1e). If there is an anomalous difference peak corresponding to an ion in the Ca^{2+}-binding pocket and it is stronger than those of sulfur in the anomalous difference Fourier map, the ions must be Ca^{2+}. If there is no significant anomalous difference peak corresponding to an ion in the Ca^{2+}-binding pocket or the peak is weaker than those of sulfur, the ions must be Mg^{2+}. Because many anomalous-difference Fourier peaks from sulfurs in cysteine and methionine residues were observed, but no notable peaks in the Ca^{2+}-binding loops of CaM, the observed ions in the Ca^{2+}-binding loops of CaM are Mg^{2+}, not Ca^{2+}. To validate this finding, I isolated a crystal grown in the absence of Ca^{2+} and EGTA and soaked it in crystallization solution containing 5 mM Ca^{2+} for 45 min before flash freezing. I then collected data at a long wavelength (1.6 Å). The Ca^{2+}- soaked crystal showed one strong (~7.5σ) and one weak (~4σ) anomalous difference peak. The strong peak was much stronger than those from cysteines and methionines (~4σ) (Figure 31B), suggesting that Ca^{2+} was successfully incorporated into the Ca^{2+}-binding loop of CaM. There were no notable structural

changes with Ca^{2+} binding. Structures of Ca^{2+}-CaM alone show that the acidic residues (Glu105 and Glu141) on the EF hands are involved in coordination of Ca^{2+} (Figure 31). In our crystal structure, the acidic residues are away from the Ca^{2+}-binding loops, probably because the structure was captured in the apo-CaM conformation (Figure 31B). However, the Ca^{2+}-binding loop in the crystal still has a preference for Ca^{2+} over Mg^{2+} as a lower concentration of Ca^{2+} (5 mM) is enough to replace a high concentration of Mg^{2+} (100 mM). With our crystallographic approach we also queried whether the EF hand of the Na_V CTD could bind Ca^{2+}. Ca^{2+} regulates Na_V channel function but whether it is through Ca^{2+}-CaM or direct binding of Ca^{2+} to a putative EF hand in the Na_V CTD has been controversial (Chagot et al. 2009; Kim et al. 2004; Miloushev et al. 2009; Shah et al. 2006). From the Ca^{2+}-soaked crystal, I observed no anomalous difference peak in the putative Ca^{2+}-binding loops of the EF hand of the Na_V CTD (Figure 31C), and there was no peak in the putative Ca^{2+}-binding loops of the EF-hand in a $2F_O$-F_C map (Figure 32). This observation is consistent with the idea that any Ca^{2+}-dependent regulation of Na_V channels occurs through the bound CaM.

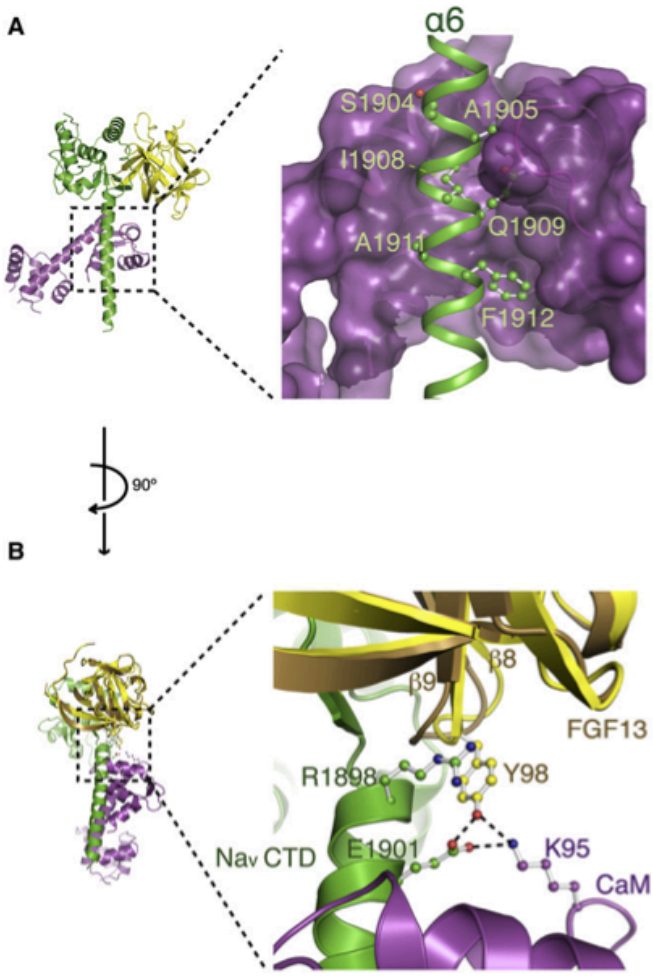

Figure 30: Interactions Of Na_v CTD With CaM And FGF13

Zoomed-in view of the interactions of the $Na_V1.5$ CTD (green) with the C-lobe of CaM (magenta) shown on the right. The ternary complex structure on the left is shown to help orient the figure on the right. The amino acids of the $Na_V1.5$ CTD involved in interactions with CaM are labeled. (B) Zoomed-in view of the ternary interactions of the $Na_V1.5$ CTD (green), FGF13 (yellow), and CaM (magenta). The structure of FGF13 obtained in the absence of binding partners (PDB ID: 3HBW) is colored brown, showing the structural change upon formation of the complex.

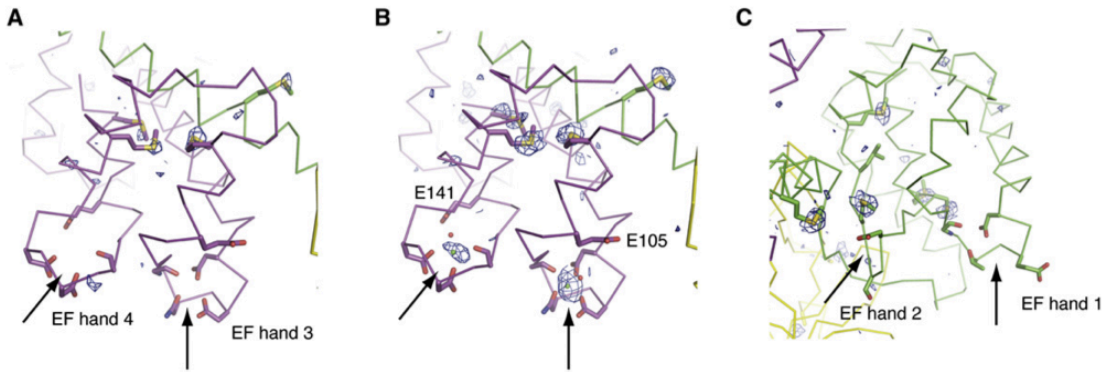

Figure 31: Anomalous Diffraction Studies Of The CaM C-lobe And Na_v CTD

Anomalous difference Fourier electron density maps of the CaM-C-lobe region from the crystals grown in the presence of EGTA **(A)** and grown in the absence of EGTA and soaked with 5 mM Ca^{2+} **(B)** are contoured at 3σ and 3.5σ, respectively. Side chains involved in Ca^{2+} coordination in the Ca^{2+}-binding loops of EF hands as well as methionine residues are shown. **(C)** Anomalous difference Fourier electron density maps of the $Na_V1.5$ CTD region from the same crystal as **(B)** contoured at 3.5σ.

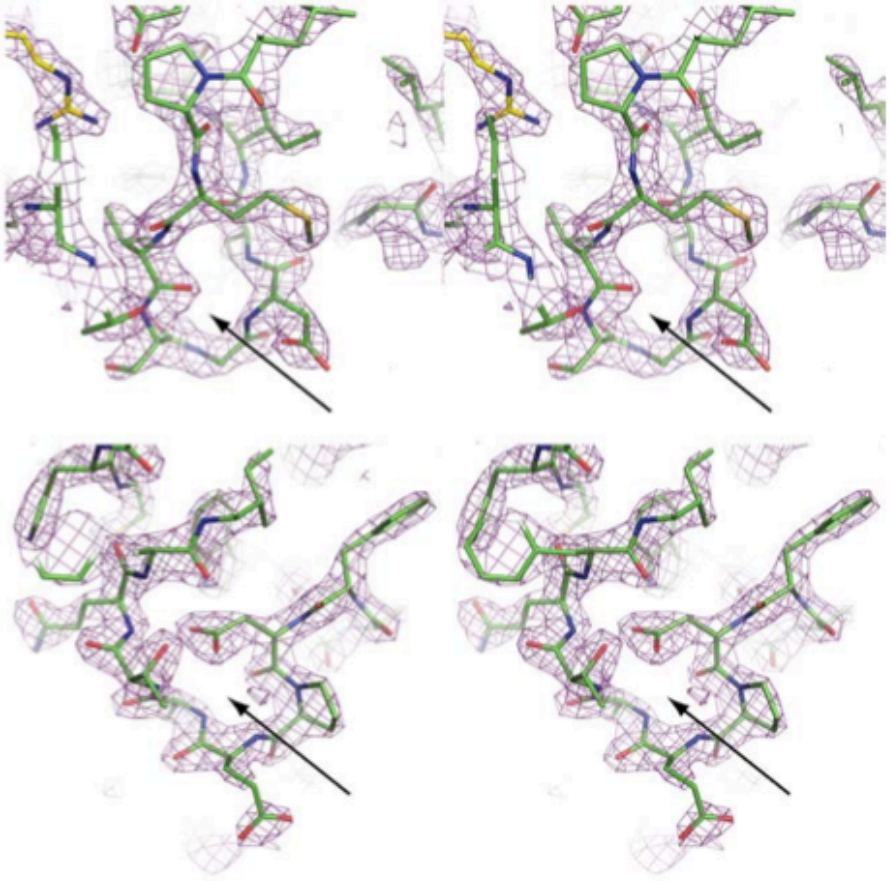

Figure 32: $2F_O$-F_C Electron Density Maps Of The Paired EF Hand Fold Region Of The Na_v CTD Fragment

$2F_O$-F_C Electron density maps of the paired EF Hand fold region of the Na_v CTD fragment (α1-α4) from the crystal structure of the ternary complex grown in the presence of 5 mM EGTA.

2.3.1.4 Ternary Interactions Among Na_v CTD, FHF, And Calmodulin

Superimposition of the FGF13 structure from the ternary complex onto the FGF13 structure obtained in the absence of binding partners (Goetz et al. 2009) shows localized structural changes around the loop between β8 and β9 (Figure 30B). Upon binding the Na_V CTD and CaM, that loop is reoriented so that Tyr98 of FGF13 interacts with Arg1898 and Glu1901 of α6 in $Na_V1.5$ via a cation-π interaction (Gallivan and Dougherty 1999) and a hydrogen bond interaction, respectively (Figure 30B). Interestingly, Glu1901 in the $Na_V1.5$ CTD as well as Tyr98 of FGF13 also are within hydrogen bonding distances of Lys95 of the third Ca^{2+}-binding EF-hand in the CaM C-lobe (Figure 30B). Mutation of Arg1902 in $Na_V1.2$, homologous to Arg1898 in $Na_V1.5$, is associated with familial autism (Weiss et al. 2003) and affects the Ca^{2+}-dependence of the interaction between the $Na_V1.2$ CTD and CaM (Kim et al. 2004; Weiss et al. 2003). It is the only site within the ternary complex containing components of all three molecules.

2.3.2 Materials And Methods

2.3.2.1 Molecular Cloning, Protein Complex Expression And Purification

The following plasmids, for protein expression and purification, have been previously described: for crystallization the human $Na_V1.5$ CTD (amino acids 1773–1940) was cloned into pET28 (Novagen) (Kim et al. 2004), the human FGF13U (accession NM_033642) was cloned into the second multiple cloning site of pETDuet-1 (Novagen) (C. Wang, Wang, et al. 2011), and CaM was cloned into pSGC02 (Kim et al. 2004). For isothermal titration calorimetry, human FGF12B (accession NM_004113) and human $Na_V1.1$ CTD (amino acids 1789–1948) were cloned into pET28 (C. Wang, Wang, et al. 2011).

The three plasmids containing the His_6-Na_V CTD, FGF, and CaM were electroporated into BL-21 (DE3) cells. Proteins were expressed after induction with 1 mM isopropyl-1-thio-β-D-galactopyranoside (IPTG) for 64 hrs at 16°C. For expression of selenomethionine incorporated proteins, the cells were grown in M9 medium with the following additions (mg/L): 100 lysine, phenylalanine, and threonine; 50 isoleucine, leucine and valine; and 60 L-selenium-methionine. Cells were grown until OD600 = 0.7, and then induced with IPTG as above. Cells were harvested and resuspended in 300 mM NaCl, 20 mM Tris-HCl, 5 mM imidazole, pH 7.5, supplemented with EDTA-free protease inhibitor mixture (Roche). Cell extracts were prepared by passage twice through an Avestin homogenizer (Emulsiflex-C5, Canada) then centrifuged at 146,300 x g for 25

min. The initial purification protocol has been previously described (C. Wang et al. 2008). Additional purification was performed by gel filtration on a Superdex 200 10/300L column on an AKTA FPLC (GE Health-care) in 300 mM NaCl, 20 mM Tris-HCl, 5 mM imidazole, with 5 mM EGTA pH 7.5. Protein concentrations were determined by UV absorbance with Thermo NANODROP and were concentrated to A_{280} = 8 in above buffer for crystallization.

2.3.2.2 Crystallography

Crystals were grown by vapor diffusion with the sitting-drop method. Crystals were obtained with 20% PEG400, 100 mM magnesium acetate, and 50 mM sodium cacodylate, pH 5.3. Before flash-freezing in liquid nitrogen, the crystals were cryoprotected by gradually increasing the concentration of PEG400 in the well solution to 38% over a period of 10 min. Single anomalous dispersion phases were obtained to 2.9 Å from SeMet-substituted crystals and then the phases were extended for model building. The final model was refined to R_{work}/R_{free} = 0.210/0.227 and contains $Na_V1.5$ CTD, FGF13, CaM, 3 Mg^{2+} (two in the Ca^{2+} binding sites in CaM and one in the crystallographic contacts), and 220 waters. The final model is of good Ramachandran statistics (98% favored and 2% allowed).

The data were collected on beam lines 22ID, 22BM, and 24ID-C at the Advanced Photon Source. The data were processed using HKL2000. The data for the SeMet-substituted crystal were collected at the Se peak wavelength (0.97936 Å) and the crystal diffracted to

2.9 Å. Phases were obtained by the single anomalous dispersion technique using PHASER (McCoy et al. 2007) from the PHENIX interface (Adams et al. 2010) with a figure of merit of 0.42. Phases were extended to 2.4 Å by solvent flattening using RESOLVE (Terwilliger 2000) against the high-resolution native data (2.2 Å). Approximately 60% of the entire model was built using AutoBuild from the PHENIX interface. Further model building was done manually using COOT (Emsley and Cowtan 2004). Structure refinement was done using the high-resolution (2.2 Å) native data.

For anomalous diffraction studies, the data for the native crystal grown in the presence of EGTA were collected to 2.6 Å Bragg spacings using the rotating anode generator (Rigaku MicroMax-007 HF micro focus) at the Duke University X-ray Crystallography facility and the data for the Ca^{2+}-soaked crystals to 2.45 Å Bragg spacings were collected at a wavelength of 1.6 Å using the beam line 24ID-C at the Advanced Photon Source. At least 180 images were collected for all the data sets. Anomalous difference Fourier maps were calculated using the phases from the structure of the ternary complex using PHENIX.

2.3.2.3 Isothermal Titration Calorimetry

Experiments were performed with an ITC-200 (MicroCal) at 20°C. Solutions containing $Na_V1.5$, $Na_V1.1$, $Na_V1.5^{E1890K}$, or $Na_V1.1^{Q1904K}$ CTD (20–51 μM) were titrated with 20–30 10-μl injections of solution containing FGF12B or $FGF12B^{K9E}$ (240–510 μM). ITC experiments were repeated with different preparations and different concentrations at least three times to confirm thermodynamic parameters and stoichiometry values. The

binding isotherms were analyzed with a single site binding model using the Microcal Origin version 7.0 software package (Originlab Corporation), yielding binding enthalpy (ΔH), stoichiometry (n), entropy (ΔS), and association constant (K_a). Due to the low affinity between the single mutation and wild-type interaction, higher concentrations of FGF12B were used. Results are presented as mean ± SEM; statistical significance was assessed using a two-tailed Student's t test and was set at $p<0.05$.

2.4 Discussion

2.4.1 Ternary Complex Structure

Our crystal structure, which includes the most structured region of the CTD as well as two critical auxiliary proteins, provides a structural basis for understanding the FHF-mediated and/or CaM-dependent regulation of Na_V channels at the molecular level. Together with the recent structure of a prokaryotic Na_V channel without CTD (Payandeh et al. 2011), our ternary complex structure of Na_V/FHF/CaM will help us to understand the regulatory mechanisms of eukaryotic Na_V channels. Particularly, it provides a foundation to understand the effects of certain pathogenic mutations in Na_V channels.

Growing evidence suggests CaM, constitutively associated with the CTD of the $Ca_V1.2$ Ca^{2+} channel (Liu et al. 2010; Wahl-Schott et al. 2006), may serve as a regulator of channel biosynthesis and trafficking in several cell types (Poomvanicha et al. 2011; H.-G. Wang et al. 2007). Indeed, overexpression of CaM was shown to rescue a trafficking-defective epilepsy mutant $Na_V1.1$ channel (Rusconi et al. 2007). By analogy, therefore,

the I1922T mutation may also decrease the number of $Na_V1.1$ channels on the plasma membrane, leading to reduced $Na_V1.1$ current.

2.4.2 Interactions Among The Ternary Complex

The interface between the Na_V CTD and FHF demonstrates an uncommon model for protein-protein interactions in that critical binding components lie at the periphery of the interaction surface. "Hot-spot" residues, those that provide the most binding energy, are usually found toward the center of the interface (Clackson and Wells 1995) and are sealed from bulk solvent to provide highly energetic interactions (Bogan and Thorn 1998). The most notable interaction in our structure is the salt bridge between a Lys in the FHF and a Glu in the Na_V CTD that contributes greatly to the interaction energy and offers a means to understand the reduced interaction between FHF and $Na_V1.1$ compared to $Na_V1.5$ (Figure 30) (C. Wang, Wang, et al. 2011). In a similar manner, the cation-π interaction between Tyr98 of FGF13 and Arg1898 (Figure 26B and Figure 26B) provides another contact point at the periphery of the main interface that may have important functional significance for Ca^{2+}-regulation through a hydrogen bond between Tyr98 of FGF13 and Lys95 of the third Ca^{2+}-binding EF-hand in the CaM C-lobe (Figure 26B). Mutation of the homologous residue in the neuronal $Na_V1.2$ (Arg1902) to cysteine, predicted to disrupt the cation-π interaction, is associated with familial autism (Weiss et al. 2003) and affects the Ca^{2+}- dependence of the interaction between the $Na_V1.2$ CTD and CaM (Kim et al. 2004; Weiss et al. 2003). Together, these observations suggest an intriguing possibility that the ternary interactions, including the cation-π interaction

between the Na_V CTD and FGF13, may serve as a critical mediator between Ca^{2+}/CaM- and FHF-mediated regulations of Na_V currents.

2.4.3 Disease-Causing Mutations Affecting Ca^{2+}-Dependent Regulation Of Na_V Function

Our data provide a context in which to consider the effects of specific disease-causing mutations in Na_V channels. Several mutations in the IQ motif of $Na_V1.1$ associated with Dravet syndrome, a severe form of childhood epilepsy, have been reported (http://www.molgen.vib-ua.be/SCN1AMutations/). The amino acids affected are within the binding sites of the proximal CaM/C-lobe or the more distal CaM/N-lobe and include Arg1927 and Arg1928, homologous to Arg1913 and Arg1914 in $Na_V1.5$ or Arg1917 and Arg1918 in $Na_V1.2$. This variant has also been reported as a recurring mutation associated with autism (O'Roak et al. 2012). Furthermore, the epilepsy-associated mutations D1866Y and T1909 in $Na_V1.1$ occur in residues that form contacts with FHF. These mutations might disrupt the FHF contacts with $Na_V1.1$, because $Na_V1.1$ appears to have a decreased affinity for FHFs compared to $Na_V1.5$ (C. Wang, Hennessey, et al. 2011). Besides, the Brugada Syndrome S1904L mutation in $Na_V1.5$ may also lead to a reduced number of $Na_V1.5$ channels and/or Na^+ current (Table 5). This would agree with the loss-of-function consequences of functionally characterized $Na_V1.5$ Brugada Syndrome mutations (Antzelevitch et al. 2005).

In addition to the mutations on Na_V, mutations in FGF12 or FGF14 prevent targeting of these FHFs and Na_V channels to the axon initial segment (Laezza et al. 2007; C. Wang,

Hennessey, et al. 2011). Accordingly, an $Na_V1.1$ epilepsy mutation that disrupts interactions with FHF might induce a loss-of-function phenotype, consistent with the proposed model in which $Na_V1.1$ mutations cause epilepsy (Catterall, Kalume, and Oakley 2010). Our structure also offers a possible explanation for the epilepsy mutation I1922T (Harkin et al. 2007), which alters a key residue for the interaction with CaM (Figure 30).

References

Adams, Paul D, Pavel V Afonine, Gábor Bunkóczi, Vincent B Chen, Ian W Davis, Nathaniel Echols, Jeffrey J Headd, et al. 2010. "PHENIX: a Comprehensive Python-Based System for Macromolecular Structure Solution.." *Acta Crystallographica. Section D, Biological Crystallography* 66 (Pt 2) (February): 213–221. doi:10.1107/S0907444909052925.

Al-Dabbagh, Bayan, Xavier Henry, Meriem El Ghachi, Geneviève Auger, Didier Blanot, Claudine Parquet, Dominique Mengin-Lecreulx, and Ahmed Bouhss. 2008. "Active Site Mapping of MraY, a Member of the Polyprenyl-Phosphate N-Acetylhexosamine 1-Phosphate Transferase Superfamily, Catalyzing the First Membrane Step of Peptidoglycan Biosynthesis† - Biochemistry (ACS Publications)." *Biochemistry* 47 (34) (August 26): 8919–8928. doi:10.1021/bi8006274.

Amer, A O, and M A Valvano. 2001. "Conserved Amino Acid Residues Found in a Predicted Cytosolic Domain of the Lipopolysaccharide Biosynthetic Protein WecA Are Implicated in the Recognition of UDP-N-Acetylglucosamine.." *Microbiology (Reading, England)* 147 (Pt 11) (November): 3015–3025.

Antzelevitch, Charles, Pedro Brugada, Martin Borggrefe, Josep Brugada, Ramon Brugada, Domenico Corrado, Ihor Gussak, et al. 2005. "Brugada Syndrome: Report of the Second Consensus Conference: Endorsed by the Heart Rhythm Society and the European Heart Rhythm Association.." In, 111:659–670. doi:10.1161/01.CIR.0000152479.54298.51.

Baker, N A, D Sept, S Joseph, M J Holst, and J A McCammon. 2001. "Electrostatics of Nanosystems: Application to Microtubules and the Ribosome.." *Proceedings of the National Academy of Sciences of the United States of America* 98 (18) (August 28): 10037–10041. doi:10.1073/pnas.181342398.

Bankston, John R, Kevin J Sampson, Suneel Kateriya, Ian W Glaaser, David L Malito, Wendy K Chung, and Robert S Kass. 2007. "A Novel LQT-3 Mutation Disrupts an Inactivation Gate Complex with Distinct Rate-Dependent Phenotypic Consequences.." *Channels (Austin, Tex.)* 1 (4) (July): 273–280.

Benhorin, J, M Goldmit, J W MacCluer, J Blangero, R Goffen, A Leibovitch, A Rahat, et al. 1998. "Identification of a New SCN5A Mutation, D1840G, Associated with the Long QT Syndrome. Mutations in Brief No. 153. Online.." *Human Mutation* 12 (1): 72. doi:10.1002/(SICI)1098-1004(1998)12:1<72::AID-HUMU19>3.0.CO;2-T.

Bogan, A A, and K S Thorn. 1998. "Anatomy of Hot Spots in Protein Interfaces.." *Journal of Molecular Biology* 280 (1) (July 3): 1–9. doi:10.1006/jmbi.1998.1843.

Bouhss, A, D Mengin-Lecreulx, D Le Beller, and J Van Heijenoort. 1999. “Topological Analysis of the MraY Protein Catalysing the First Membrane Step of Peptidoglycan Synthesis..” *Molecular Microbiology* 34 (3) (November): 576–585.

Bouhss, Ahmed, Amy E Trunkfield, Timothy D H Bugg, and Dominique Mengin-Lecreulx. 2008. “The Biosynthesis of Peptidoglycan Lipid-Linked Intermediates.” *FEMS Microbiology Reviews* 32 (2) (March): 208–233. doi:10.1111/j.1574-6976.2007.00089.x.

Bugg, Timothy D H, Darren Braddick, Christopher G Dowson, and David I Roper. 2011. “Bacterial Cell Wall Assembly: Still an Attractive Antibacterial Target..” *Trends in Biotechnology* 29 (4) (April): 167–173. doi:10.1016/j.tibtech.2010.12.006.

Catterall, William A, Franck Kalume, and John C Oakley. 2010. “NaV1.1 Channels and Epilepsy..” *The Journal of Physiology* 588 (Pt 11) (June 1): 1849–1859. doi:10.1113/jphysiol.2010.187484.

Chagot, Benjamin, and Walter J Chazin. 2011. “Solution NMR Structure of Apo-Calmodulin in Complex with the IQ Motif of Human Cardiac Sodium Channel NaV1.5.” *Journal of Molecular Biology* 406 (1) (February 11): 106–119. doi:10.1016/j.jmb.2010.11.046.

Chagot, Benjamin, Franck Potet, Jeffrey R Balser, and Walter J Chazin. 2009. “Solution NMR Structure of the C-Terminal EF-Hand Domain of Human Cardiac Sodium Channel NaV1.5..” *The Journal of Biological Chemistry* 284 (10) (March 6): 6436–6445. doi:10.1074/jbc.M807747200.

Clackson, T, and J A Wells. 1995. “A Hot Spot of Binding Energy in a Hormone-Receptor Interface..” *Science (New York, NY)* 267 (5196) (January 20): 383–386.

Davies, Julian, and Dorothy Davies. “Origins and Evolution of Antibiotic Resistance.” *Mmbr.Asm.org*.

de Kruijff, Ben, Vincent van Dam, and Eefjan Breukink. 2008. “Lipid II: a Central Component in Bacterial Cell Wall Synthesis and a Target for Antibiotics..” *Prostaglandins, Leukotrienes, and Essential Fatty Acids* 79 (3-5) (September): 117–121. doi:10.1016/j.plefa.2008.09.020.

Elena Bogatcheva, Tia Dubuisson Marina Protopopova Leo Einck Carol A Nacy Venkata M Reddy. 2011. “Chemical Modification of Capuramycins to Enhance Antibacterial Activity.” *Journal of Antimicrobial Chemotherapy* 66 (3) (March 1): 578. doi:10.1093/jac/dkq495.

Emsley, Paul, and Kevin Cowtan. 2004. “Coot: Model-Building Tools for Molecular

Graphics..” *Acta Crystallographica. Section D, Biological Crystallography* 60 (Pt 12 Pt 1) (December): 2126–2132. doi:10.1107/S0907444904019158.

Feldkamp, Michael D, Liping Yu, and Madeline A Shea. 2011. “Structural and Energetic Determinants of Apo Calmodulin Binding to the IQ Motif of the Na(v)1.2 Voltage-Dependent Sodium Channel..” *Structure* 19 (5) (May 11): 733–747. doi:10.1016/j.str.2011.02.009.

Fox, Brian G, and Paul G Blommel. 2009. “Autoinduction of Protein Expression..” *Current Protocols in Protein Science / Editorial Board, John E. Coligan ... [Et Al.]* Chapter 5 (April): Unit 5.23. doi:10.1002/0471140864.ps0523s56.

Gallivan, J P, and D A Dougherty. 1999. “Cation-Pi Interactions in Structural Biology..” *Proceedings of the National Academy of Sciences of the United States of America* 96 (17) (August 17): 9459–9464.

Goetz, Regina, Katarzyna Dover, Fernanda Laezza, Nataly Shtraizent, Xiao Huang, Dafna Tchetchik, Anna V Eliseenkova, et al. 2009. “Crystal Structure of a Fibroblast Growth Factor Homologous Factor (FHF) Defines a Conserved Surface on FHFs for Binding and Modulation of Voltage-Gated Sodium Channels..” *The Journal of Biological Chemistry* 284 (26) (June 26): 17883–17896. doi:10.1074/jbc.M109.001842.

Goldfarb, Mitchell, Jon Schoorlemmer, Anthony Williams, Shyam Diwakar, Qing Wang, Xiao Huang, Joanna Giza, et al. 2007. “Fibroblast Growth Factor Homologous Factors Control Neuronal Excitability Through Modulation of Voltage-Gated Sodium Channels..” *Neuron* 55 (3) (August 2): 449–463. doi:10.1016/j.neuron.2007.07.006.

Harkin, Louise A, Jacinta M McMahon, Xenia Iona, Leanne Dibbens, James T Pelekanos, Sameer M Zuberi, Lynette G Sadleir, et al. 2007. “The Spectrum of SCN1A-Related Infantile Epileptic Encephalopathies..” *Brain : a Journal of Neurology* 130 (Pt 3) (March): 843–852. doi:10.1093/brain/awm002.

Haug, K, K Hallmann, J Rebstock, J Dullinger, S Muth, F Haverkamp, H Pfeiffer, et al. 2001. “The Voltage-Gated Sodium Channel Gene SCN2A and Idiopathic Generalized Epilepsy..” *Epilepsy Research* 47 (3) (December): 243–246.

Heydanek, M G, W G Struve, and F C Neuhaus. 1969. “On the Initial Stage in Peptidoglycan Synthesis. 3. Kinetics and Uncoupling of Phospho-N-Acetylmuramyl-Pentapeptide Translocase (Uridine 5'-Phosphate)..” *Biochemistry* 8 (3) (March): 1214–1221.

Hidalgo, P, and R MacKinnon. 1995. “Revealing the Architecture of a K+ Channel Pore Through Mutant Cycles with a Peptide Inhibitor..” *Science (New York, NY)* 268

(5208) (April 14): 307–310.

Jiang, Youxing, Alice Lee, Jiayun Chen, Vanessa Ruta, Martine Cadene, Brian T Chait, and Roderick MacKinnon. 2003. “X-Ray Structure of a Voltage-Dependent K+ Channel..” *Nature* 423 (6935) (May 1): 33–41. doi:10.1038/nature01580.

Kapplinger, Jamie D, David J Tester, Marielle Alders, Begoña Benito, Myriam Berthet, Josep Brugada, Pedro Brugada, et al. 2010. “An International Compendium of Mutations in the SCN5A-Encoded Cardiac Sodium Channel in Patients Referred for Brugada Syndrome Genetic Testing..” *Heart Rhythm : the Official Journal of the Heart Rhythm Society* 7 (1) (January): 33–46. doi:10.1016/j.hrthm.2009.09.069.

Kim, James, Smita Ghosh, Huajun Liu, Michihiro Tateyama, Robert S Kass, and Geoffrey S Pitt. 2004. “Calmodulin Mediates Ca2+ Sensitivity of Sodium Channels..” *The Journal of Biological Chemistry* 279 (43) (October 22): 45004–45012. doi:10.1074/jbc.M407286200.

Kurosu, Michio, Kai Li, and Dean C Crick. 2009. “Concise Synthesis of Capuramycin..” *Organic Letters* 11 (11) (June 4): 2393–2396. doi:10.1021/ol900458w.

Laezza, Fernanda, Benjamin R Gerber, Jun-Yang Lou, Marie A Kozel, Hali Hartman, Ann Marie Craig, David M Ornitz, and Jeanne M Nerbonne. 2007. “The FGF14(F145S) Mutation Disrupts the Interaction of FGF14 with Voltage-Gated Na+ Channels and Impairs Neuronal Excitability..” *The Journal of Neuroscience : the Official Journal of the Society for Neuroscience* 27 (44) (October 31): 12033–12044. doi:10.1523/JNEUROSCI.2282-07.2007.

Lawrence, M C, and P M Colman. 1993. “Shape Complementarity at Protein/Protein Interfaces..” *Journal of Molecular Biology* 234 (4) (December 20): 946–950. doi:10.1006/jmbi.1993.1648.

Lee, Seok-Yong, Alice Lee, Jiayun Chen, and Roderick MacKinnon. 2005. “Structure of the KvAP Voltage-Dependent K+ Channel and Its Dependence on the Lipid Membrane..” *Proceedings of the National Academy of Sciences of the United States of America* 102 (43) (October 25): 15441–15446. doi:10.1073/pnas.0507651102.

Lehrman, M A. 1994. “A Family of UDP-GlcNAc/MurNAc: Polyisoprenol-P GlcNAc/MurNAc-1-P Transferases..” *Glycobiology* 4 (6) (December): 768–771.

Liu Cj, S D Dib-Hajj, and S G Waxman. 2001. “Fibroblast Growth Factor Homologous Factor 1B Binds to the C Terminus of the Tetrodotoxin-Resistant Sodium Channel rNav1.9a (NaN)..” *The Journal of Biological Chemistry* 276 (22) (June 1): 18925–18933. doi:10.1074/jbc.M101606200.

Liu, Xiaodong, Philemon S Yang, Wanjun Yang, and David T Yue. 2010. “Enzyme-Inhibitor-Like Tuning of Ca(2+) Channel Connectivity with Calmodulin..” *Nature* 463 (7283) (February 18): 968–972. doi:10.1038/nature08766.

Lloyd, Adrian J, Philip E Brandish, Andrea M Gilbey, and Timothy D H Bugg. 2004. “Phospho-N-Acetyl-Muramyl-Pentapeptide Translocase From Escherichia Coli: Catalytic Role of Conserved Aspartic Acid Residues..” *Journal of Bacteriology* 186 (6) (March): 1747–1757.

Long, Stephen B, Ernest B Campbell, and Roderick MacKinnon. 2005. “Voltage Sensor of Kv1.2: Structural Basis of Electromechanical Coupling..” *Science (New York, NY)* 309 (5736) (August 5): 903–908. doi:10.1126/science.1116270.

Lossin, Christoph. 2009. “A Catalog of SCN1A Variants..” *Brain & Development* 31 (2) (February): 114–130. doi:10.1016/j.braindev.2008.07.011.

McCoy, Airlie J, Ralf W Grosse-Kunstleve, Paul D Adams, Martyn D Winn, Laurent C Storoni, and Randy J Read. 2007. “Phaser Crystallographic Software..” *Journal of Applied Crystallography* 40 (Pt 4) (August 1): 658–674. doi:10.1107/S0021889807021206.

Meisler, Miriam H, Janelle E O'Brien, and Lisa M Sharkey. 2010. “Sodium Channel Gene Family: Epilepsy Mutations, Gene Interactions and Modifier Effects..” *The Journal of Physiology* 588 (Pt 11) (June 1): 1841–1848. doi:10.1113/jphysiol.2010.188482.

Mendel, Sharon, Joanne M Holbourn, James A Schouten, and Timothy D H Bugg. 2006. “Interaction of the Transmembrane Domain of Lysis Protein E From Bacteriophage phiX174 with Bacterial Translocase MraY and Peptidyl-Prolyl Isomerase SlyD..” *Microbiology (Reading, England)* 152 (Pt 10) (October): 2959–2967. doi:10.1099/mic.0.28776-0.

Miloushev, Vesselin Z, Joshua A Levine, Mark A Arbing, John F Hunt, Geoffrey S Pitt, and Arthur G Palmer. 2009. “Solution Structure of the NaV1.2 C-Terminal EF-Hand Domain..” *The Journal of Biological Chemistry* 284 (10) (March 6): 6446–6454. doi:10.1074/jbc.M807401200.

Mori, Masayuki, Takashi Konno, Takashi Morii, Kuniaki Nagayama, and Keiji Imoto. 2003. “Regulatory Interaction of Sodium Channel IQ-Motif with Calmodulin C-Terminal Lobe..” *Biochemical and Biophysical Research Communications* 307 (2) (July 25): 290–296.

Nikonenko, B V, V M Reddy, M Protopopova, E Bogatcheva, L Einck, and C A Nacy. 2009. “Activity of SQ641, a Capuramycin Analog, in a Murine Model of

Tuberculosis." *Antimicrobial Agents and Chemotherapy* 53 (7) (June 24): 3138–3139. doi:10.1128/AAC.00366-09.

O'Roak, Brian J, Laura Vives, Wenqing Fu, Jarrett D Egertson, Ian B Stanaway, Ian G Phelps, Gemma Carvill, et al. 2012. "Multiplex Targeted Sequencing Identifies Recurrently Mutated Genes in Autism Spectrum Disorders.." *Science (New York, NY)* 338 (6114) (December 21): 1619–1622. doi:10.1126/science.1227764.

Ohmori, Iori, Kristopher M Kahlig, Thomas H Rhodes, Dao W Wang, and Alfred L George. 2006. "Nonfunctional SCN1A Is Common in Severe Myoclonic Epilepsy of Infancy.." *Epilepsia* 47 (10) (October): 1636–1642. doi:10.1111/j.1528-1167.2006.00643.x.

Olsen, Shaun K, Meirav Garbi, Niccolo Zampieri, Anna V Eliseenkova, David M Ornitz, Mitchell Goldfarb, and Moosa Mohammadi. 2003. "Fibroblast Growth Factor (FGF) Homologous Factors Share Structural but Not Functional Homology with FGFs.." *The Journal of Biological Chemistry* 278 (36) (September 5): 34226–34236. doi:10.1074/jbc.M303183200.

Payandeh, Jian, Todd Scheuer, Ning Zheng, and William A Catterall. 2011. "The Crystal Structure of a Voltage-Gated Sodium Channel.." *Nature* 475 (7356) (July 21): 353–358. doi:10.1038/nature10238.

Poomvanicha, Montatip, Jörg W Wegener, Anne Blaich, Stefanie Fischer, Katrin Domes, Sven Moosmang, and Franz Hofmann. 2011. "Facilitation and Ca2+-Dependent Inactivation Are Modified by Mutation of the Ca(v)1.2 Channel IQ Motif.." *The Journal of Biological Chemistry* 286 (30) (July 29): 26702–26707. doi:10.1074/jbc.M111.247841.

Reddy, V M, L Einck, and C A Nacy. 2008. "In Vitro Antimycobacterial Activities of Capuramycin Analogues." *Antimicrobial Agents and Chemotherapy* 52 (2) (January 23): 719–721. doi:10.1128/AAC.01469-07.

Roberts, Rebecca R, Bala Hota, Ibrar Ahmad, R Douglas Scott II, Susan D Foster, Fauzia Abbasi, Shari Schabowski, et al. 2009. "Hospital and Societal Costs of Antimicrobial-Resistant Infections in a Chicago Teaching Hospital: Implications for Antibiotic Stewardship." *Clinical Infectious Diseases* 49 (8) (October 15): 1175–1184. doi:10.1086/605630.

Rusconi, Raffaella, Paolo Scalmani, Rita Restano Cassulini, Giulia Giunti, Antonio Gambardella, Silvana Franceschetti, Grazia Annesi, Enzo Wanke, and Massimo Mantegazza. 2007. "Modulatory Proteins Can Rescue a Trafficking Defective Epileptogenic Nav1.1 Na+ Channel Mutant.." *The Journal of Neuroscience : the Official Journal of the Society for Neuroscience* 27 (41) (October 10): 11037–11046.

doi:10.1523/JNEUROSCI.3515-07.2007.

Rush, J S, P D Rick, and C J Waechter. 1997. “Polyisoprenyl Phosphate Specificity of UDP-GlcNAc:Undecaprenyl Phosphate N-Acetylglucosaminyl 1-P Transferase From E.Coli..” *Glycobiology* 7 (2) (March): 315–322.

Schumacher, Maria A, Matthew Crum, and Marshall C Miller. 2004. “Crystal Structures of Apocalmodulin and an Apocalmodulin/SK Potassium Channel Gating Domain Complex..” *Structure* 12 (5) (May): 849–860. doi:10.1016/j.str.2004.03.017.

Shah, Vikas N, Tammy L Wingo, Kevin L Weiss, Christina K Williams, Jeffrey R Balser, and Walter J Chazin. 2006. “Calcium-Dependent Regulation of the Voltage-Gated Sodium Channel hH1: Intrinsic and Extrinsic Sensors Use a Common Molecular Switch..” *Proceedings of the National Academy of Sciences of the United States of America* 103 (10) (March 7): 3592–3597. doi:10.1073/pnas.0507397103.

Smallwood, P M, I Munoz-Sanjuan, P Tong, J P Macke, S H Hendry, D J Gilbert, N G Copeland, N A Jenkins, and J Nathans. 1996. “Fibroblast Growth Factor (FGF) Homologous Factors: New Members of the FGF Family Implicated in Nervous System Development..” *Proceedings of the National Academy of Sciences of the United States of America* 93 (18) (September 3): 9850–9857.

Spampanato, J, J A Kearney, G de Haan, D P McEwen, A Escayg, I Aradi, B T MacDonald, et al. 2004. “A Novel Epilepsy Mutation in the Sodium Channel SCN1A Identifies a Cytoplasmic Domain for Beta Subunit Interaction..” *The Journal of Neuroscience : the Official Journal of the Society for Neuroscience* 24 (44) (November 3): 10022–10034. doi:10.1523/JNEUROSCI.2034-04.2004.

Tanaka, Shiho, and William M Clemons Jr. 2012. “Minimal Requirements for Inhibition of MraY by Lysis Protein E From Bacteriophage ΦX174.” *Molecular Microbiology* (July 13): no–no. doi:10.1111/j.1365-2958.2012.08153.x.

Tanino, Tetsuya, Bayan Al-Dabbagh, Dominique Mengin-Lecreulx, Ahmed Bouhss, Hiroshi Oyama, Satoshi Ichikawa, and Akira Matsuda. 2011. “Mechanistic Analysis of Muraymycin Analogues: a Guide to the Design of MraY Inhibitors.” *Journal of Medicinal Chemistry* 54 (24) (December 22): 8421–8439. doi:10.1021/jm200906r.

Terwilliger, T C. 2000. “Maximum-Likelihood Density Modification..” *Acta Crystallographica. Section D, Biological Crystallography* 56 (Pt 8) (August): 965–972.

Tester, David J, Melissa L Will, Carla M Haglund, and Michael J Ackerman. 2005. “Compendium of Cardiac Channel Mutations in 541 Consecutive Unrelated Patients Referred for Long QT Syndrome Genetic Testing..” *Heart Rhythm : the Official*

Journal of the Heart Rhythm Society 2 (5) (May): 507–517. doi:10.1016/j.hrthm.2005.01.020.

Tia Dubuisson, Elena Bogatcheva Manju Y Krishnan Michael T Collins Leo Einck Carol A Nacy Venkata M Reddy. 2010. "In Vitro Antimicrobial Activities of Capuramycin Analogues Against Non-Tuberculous Mycobacteria." *Journal of Antimicrobial Chemotherapy* 65 (12) (December 1): 2590. doi:10.1093/jac/dkq372.

van Swieten, John C, Esther Brusse, Bianca M de Graaf, Elmar Krieger, Raoul van de Graaf, Inge de Koning, Anneke Maat-Kievit, et al. 2003. "A Mutation in the Fibroblast Growth Factor 14 Gene Is Associated with Autosomal Dominant Cerebellar Ataxia [Corrected].." *American Journal of Human Genetics* 72 (1) (January): 191–199.

Wahl-Schott, Christian, Ludwig Baumann, Hartmut Cuny, Christian Eckert, Kristina Griessmeier, and Martin Biel. 2006. "Switching Off Calcium-Dependent Inactivation in L-Type Calcium Channels by an Autoinhibitory Domain.." *Proceedings of the National Academy of Sciences of the United States of America* 103 (42) (October 17): 15657–15662. doi:10.1073/pnas.0604621103.

Wang, Chaojian, Chuan Wang, Ethan G Hoch, and Geoffrey S Pitt. 2011. "Identification of Novel Interaction Sites That Determine Specificity Between Fibroblast Growth Factor Homologous Factors and Voltage-Gated Sodium Channels.." *The Journal of Biological Chemistry* 286 (27) (July 8): 24253–24263. doi:10.1074/jbc.M111.245803.

Wang, Chaojian, Hong-Gang Wang, Hui Xie, and Geoffrey S Pitt. 2008. "Ca2+/CaM Controls Ca2+-Dependent Inactivation of NMDA Receptors by Dimerizing the NR1 C Termini.." *The Journal of Neuroscience : the Official Journal of the Society for Neuroscience* 28 (8) (February 20): 1865–1870. doi:10.1523/JNEUROSCI.5417-07.2008.

Wang, Chuan, Jessica A Hennessey, Robert D Kirkton, Chaojian Wang, Victoria Graham, Ram S Puranam, Paul B Rosenberg, Nenad Bursac, and Geoffrey S Pitt. 2011. "Fibroblast Growth Factor Homologous Factor 13 Regulates Na+ Channels and Conduction Velocity in Murine Hearts.." *Circulation Research* 109 (7) (September 16): 775–782. doi:10.1161/CIRCRESAHA.111.247957.

Wang, Hong-Gang, Meena S George, James Kim, Chaojian Wang, and Geoffrey S Pitt. 2007. "Ca2+/Calmodulin Regulates Trafficking of Ca(v)1.2 Ca2+ Channels in Cultured Hippocampal Neurons.." *The Journal of Neuroscience : the Official Journal of the Society for Neuroscience* 27 (34) (August 22): 9086–9093. doi:10.1523/JNEUROSCI.1720-07.2007.

Wang, Qing, Mark E Bardgett, Michael Wong, David F Wozniak, Junyang Lou, Benjamin D McNeil, Chen Chen, et al. 2002. “Ataxia and Paroxysmal Dyskinesia in Mice Lacking Axonally Transported FGF14..” *Neuron* 35 (1) (July 3): 25–38.

Weiss, L A, A Escayg, J A Kearney, M Trudeau, B T MacDonald, M Mori, J Reichert, J D Buxbaum, and M H Meisler. 2003. “Sodium Channels SCN1A, SCN2A and SCN3A in Familial Autism..” *Molecular Psychiatry* 8 (2) (February): 186–194. doi:10.1038/sj.mp.4001241.

White, Courtney L, Aleksandar Kitich, and James W Gober. 2010. “Positioning Cell Wall Synthetic Complexes by the Bacterial Morphogenetic Proteins MreB and MreD..” *Molecular Microbiology* 76 (3) (May): 616–633. doi:10.1111/j.1365-2958.2010.07108.x.

Winn, Michael, Rebecca J M Goss, Ken-ichi Kimura, and Timothy D H Bugg. 2010. “Antimicrobial Nucleoside Antibiotics Targeting Cell Wall Assembly: Recent Advances in Structure-Function Studies and Nucleoside Biosynthesis..” *Natural Product Reports* 27 (2) (February): 279–304. doi:10.1039/b816215h.

Zimmer, Thomas, and Ralf Surber. 2008. “SCN5A Channelopathies--an Update on Mutations and Mechanisms..” *Progress in Biophysics and Molecular Biology* 98 (2-3) (October): 120–136. doi:10.1016/j.pbiomolbio.2008.10.005.

Biography

Chih-Pin Chung

Education and Experience

1998 – 2002 National Yang-Ming University, Taipei, Taiwan. B.S. Life Sciences, *Studies of the chromatin-remodeling complex (RSC complex) in yeast model system.*
Advisor: Ming-Yuan Cheng, M.D., Ph.D.

2003 – 2006 Academia Sinica, Institute of Biomedical Sciences, Taipei, Taiwan, Research Assistant,
NMR Solution structure of the Arabidopsis thaliana telomeric DNA binding protein
Supervisor: Tai-Huang Huang, Ph.D.

Publication

Chung, Ben C, Jinshi Zhao, Robert A Gillespie, Do-Yeon Kwon, Ziqiang Guan, Jiyong Hong, Pei Zhou, and Seok-Yong Lee. 2013. "Crystal Structure of MraY, an Essential Membrane Enzyme for Bacterial Cell Wall Synthesis.." *Science (New York, NY)* 341 (6149) (August 30): 1012–1016. doi:10.1126/science.1236501.

Wang, Chaojian, Ben C Chung, Haidun Yan, Seok-Yong Lee, and Geoffrey S Pitt. 2012. "Crystal Structure of the Ternary Complex of a NaV C-Terminal Domain, a Fibroblast Growth Factor Homologous Factor, and Calmodulin." *Structure* 20 (7) (July): 1167–1176. doi:10.1016/j.str.2012.05.001.

Sue, Shih-Che, Hsin-Hao Hsiao, Ben C-P Chung, Ying-Hsien Cheng, Kuang-Lung Hsueh, Chung Mong Chen, Chia Hsing Ho, and Tai-Huang Huang. 2006. "Solution Structure of the Arabidopsis Thaliana Telomeric Repeat-Binding Protein DNA Binding Domain: a New Fold with an Additional C-Terminal Helix.." *Journal of Molecular Biology* 356 (1) (February 10): 72–85. doi:10.1016/j.jmb.2005.11.009.